All-optical signatures of quantum vacuum nonlinearities in numerical simulations of unexplored regimes

Lars Maiwald (*15.11.1999 in Weimar)

Arbeit zur Erlangung des akademischen Grades

Master of Science im Fach Physik

Friedrich-Schiller-Universität Jena
Physikalisch-Astronomische Fakultät
Theoretisch-Physikalisches Institut

Erstgutachter:

Prof. Dr. Holger Gies
Theoretisch-Physikalisches Institut
Friedrich-Schiller-Universität Jena

Zweitgutachter:

Dr. Felix Karbstein
Helmholtz Institute Jena
Theoretisch-Physikalisches Institut
Friedrich-Schiller-Universität Jena

Abstract

Quantum electrodynamics predicts nonlinear interactions of electromagnetic fields. Vacuum fluctuations mediate this interaction. These quantum vacuum nonlinearities supplement Maxwell's theory but only become relevant for strong electromagnetic fields. Even at leading high-intensity laser facilities, these phenomena remain elusive and are therefore yet to be tested.
Precision tests of the theory require accurate predictions of the signatures of quantum vacuum nonlinearities. The vacuum emission picture allows for an efficient theoretical treatment in terms of a single photon emission process. Realistic electromagnetic fields lead to difficulties in analytically calculating the zero-to-one signal photon transition amplitude. The VacEm code by Blinne provides a tool for numerical simulations of the signal for arbitrary field profiles.
This work contains a detailed analysis of the VacEm code, improves it, and employs it for an analytically inaccessible system. Reformulating the signal amplitude to allow for efficient numerical computation provides the foundation for understanding the algorithm, code structure, and workflow. Computational cost is the only limiting factor for the simulations. When balancing resource usage and result accuracy, numerical artifacts are of great importance and therefore are analyzed extensively. Furthermore, code improvements are implemented to reduce both memory usage and computation time. They enable a short study of scattering two counterpropagating flat top pulses, one featuring a field-free hole in its center. Despite their hard-to-resolve field profiles, the presumed signal features are found. A partial workaround for the inevitable numerical artifacts is shown using extrapolation and successfully mimics infinite simulation spacetime volume.

Quantenelektrodynamik sagt nichtlineare Interaktionen von elektromagnetischen Felder voraus. Vakuumfluktuationen vermitteln diese Interaktionen. Diese Quantenvakuum-Nichtlinearitäten ergänzen Maxwells Theorie. Relevanz erreichen sie jedoch erst bei hohen Feldstärken. Aus diesem Grund ist ihr Nachweis selbst an den führenden Hochintensitäts-Lasereinrichtungen eine große Herausforderung und bleibt zu erbringen.
Präzisionstests der Theorie erfordern genaue Vorhersagen der Signaturen von Quantenvakuum-Nichtlinearitäten. Das Vacuum Emission Picture bewerkstelligt eine effiziente theoretische Behandlung als 1-Photonen-Emissionsprozess. Realistische elektromagnetische Felder führen allerdings zu Schwierigkeiten bei der analytischen Berechnung der 0-zu-1 Signalphotonen-Übergangsamplitude. Der VacEm-Code von Blinne ist ein numerischer Simulationscode des Signals für

beliebige Feldprofile.

Diese Arbeit enthält eine detaillierte Analyse des VacEm-Codes, verbessert ihn und setzt ihn zur Simulation eines analytisch unzugänglichen Systems ein. Eine Neuformulierung der Signalamplitude gestattet ihre effiziente numerische Berechnung. Das ist die Grundlage für das Verständnis des Code-Algorithmus, seiner Struktur und möglicher Workflows. Rechenaufwand ist der einzige limitierende Faktor für die Simulationen. Bei der Balance zwischen Ressourcennutzung und Ergebnisgenauigkeit spielen numerische Artefakte die zentrale Rolle. Sie werden darum ausführlich untersucht. Des Weiteren werden Code-Verbesserungen implementiert, die sowohl RAM-Nutzung als auch Rechenzeit reduzieren. Die Verbesserungen ermöglichen eine kleine Untersuchung der Streuung zweier gegenläufiger Flat-Top-Pulse, einer mit einem zentralen feldfreien Loch. Trotz der schwer aufzulösenden Feldprofile wird das vermutete Signalverhalten gefunden. Für die unausweichlichen numerischen Artefakte wird ein partieller Workaround gezeigt, der erfolgreich zu einem unendlich großen Simulationsvolumen extrapoliert.

Contents

1 Introduction

1873: James Clerk Maxwell publishes *A Treatise on Electricity and Magnetism* [1] laying the foundation for countless technologies that shape our world. The precise mathematical study of electric and magnetic fields contained in his work lives on in the form of Maxwell's equations.

> "From a long view of the history of mankind - seen from, say, ten thousand years from now - there can be little doubt that the most significant event of the 19th century will be judged as Maxwell's discovery of the laws of electrodynamics. The American Civil War will pale into provincial insignificance in comparison with this important scientific event of the same decade." (Feynman 1964 [2])

Maxwell's theory (ED) accurately describes the behavior of macroscopic electromagnetic fields and enables applications from radar to wireless communication. Nevertheless, with the advent of the age of quantum theories the limitations of Maxwell's classical theory became visible. Quantum electrodynamics (QED) [3], not to be seen as a replacement for ED but simply as the relativistic quantum field theory of electrodynamics, allows for extremely accurate predictions [4] and descriptions of phenomena like the photoelectric effect or photon-photon scattering, incompatible with ED. Whether QED will ever become technologically as relevant as ED remains to be seen. Regardless, the scientific potential is immense. Concerning this work, it provides a suitable tool in the study of quantum vacuum physics. The quantum vacuum state is the state with the lowest energy possible. Contrary to naive assumption, the quantum vacuum is neither empty nor simple. It is a complex state governed by quantum fluctuations (vacuum fluctuations), *i.e.* fluctuations in the values measured for field amplitudes and conjugate momenta due to Heisenberg's uncertainty principle. In particular, the term quantum fluctuations refers to the virtual processes quantified by Feynman diagrams and occurring in the quantum vacuum. For the context at hand the picture of constant creation and annihilation of virtual particle-antiparticle pairs is useful.

QED can be used to probe the quantum vacuum [5]. The vacuum of QED is particularly interesting to study because of its accessibility. In probing the quantum vacuum, it is necessary to excite the fluctuations. This can straightforwardly be achieved in QED using strong external EM fields, thanks to the advances in laser physics [6–10]. The research in this area started with the work of Heisenberg and Euler in 1935/36 [11, 12]. They derived the effective action describing the quantum vacuum nonlinearities of QED to 1-loop order (Heisenberg-Euler effective action). This defines the foundation for this work and a lot of research in the field; see [13–16] for recent

reviews.

Maxwell's equations in vacuum are linear, there is no coupling between EM fields. Nonlinearities only appear in the quantum vacuum and are parametrically suppressed by the reduced Planck's constant $\hbar$ [17]. They are higher order corrections to the linear Maxwell action, which brings us back to our starting point of Maxwell's theory. The nonlinearities are a pure quantum effect, a property of the medium which is the quantum vacuum, theoretically predicted and experimentally elusive. Further theoretical study is of great importance in guiding the experiments. Successful experiments would verify QED in the yet untested regime of low-energy quantum vacuum properties and advance the quantum vacuum research. Promising signatures of quantum vacuum nonlinearities are vacuum birefringence [18–30], light-by-light scattering [11, 12, 31–43], photon merging [44–46], photon splitting [18, 19, 47–52], and higher-harmonic generation [53–57].

In 2015 Karbstein and Shaisultanov [58] developed the vacuum emission picture (VEP) allowing for a clean theoretical study of the QED quantum vacuum nonlinearities in terms of the single photon emission process. The process of interest is the interaction of three external (classical) background photons via quantum fluctuations (virtual electrons and positrons) to create one (quantum) signal photon. The VEP allows us to write down an expression for the transition amplitude from the vacuum to the single photon state. Analytical studies, working in the VEP, can be found in *e.g.* [17, 59, 60]. To expand on the situations that allow for analytical study and explore analytically inaccessible regimes, numerical simulations become necessary. A successful approach was developed by Blinne *et al.* in [61].

Our goal is to expand on the work in [61] by studying the possibilities and limitations of the numerical simulation code developed by Blinne. Furthermore, we use our adapted version of the code to study the counterpropagating collision of two pulses, which can be described in the far field as one flat top pump pulse and one flat top probe pulse featuring a centered field-free hole. We do so taking inspiration from [17]. When studying the signal produced in the scattering process, we investigate the dependence of the signal photon emission direction on the beam waist radius of the pump.

Our work builds on the established analytical research within VEP and is done by high-performance computing (HPC) numerical simulations written in `Python`. The computational resources are provided by the HPC-cluster *Draco* of *FSU* Jena [62].

In section 2 we give the necessary theoretical background for this work, mainly focusing on the VEP. Section 3 provides an in-depth view on the numerical simulation code by Blinne, looks

into numerical artifacts and explains our performance improvements. Equipped with the theoretical understanding of the topic and the vacuum emission code we study flat top scattering in section 4.

2 Vacuum emission picture

The quantum vacuum is the ground state of a quantum system, *i.e.* the state of the lowest energy (zero-point energy). We focus exclusively on the QED sector which contains the electromagnetic field and the electron-positron field. Quantum fluctuations are ever-present in both fields and govern the properties of the vacuum. The picture of the QED vacuum as a medium with constant creation and mutual annihilation of electron-positron pairs is useful. Considering the quantum vacuum as a medium, it is natural to expect corrections to the vacuum ED action.

2.1 Heisenberg-Euler effective action

Heisenberg and Euler published *Folgerungen aus der Diracschen Theorie des Positrons* [12] in 1936. They derive the effective Lagrangian for QED with classical EM field background to 1-loop order. The starting point is given by the custom QED Lagrangian

$$\mathcal{L} = \bar{\psi}\mathrm{i}\gamma_\mu \left(\partial_\mu - \mathrm{i}eA^\mu\right)\psi - m_e\bar{\psi}\psi - \frac{1}{4}F_{\mu\nu}F^{\mu\nu}\,, \tag{2.1}$$

with Dirac spinor ψ of the electron-positron field, Dirac adjoint $\bar{\psi}$, gamma matrices γ_μ, four-potential A^μ, elementary charge e, electron mass m_e, and field strength tensor $F_{\mu\nu} = \partial_\mu A_\nu - \partial_\nu A_\mu$. We have fermionic degrees of freedom (DOF) $\bar{\psi}, \psi$, no bosonic DOF, but a classical (external) EM background field A^μ ($F_{\mu\nu}$). The result of Heisenberg and Euler, now known as the Heisenberg-Euler effective Lagrangian $\mathcal{L}_{\mathrm{HE}}$, is given by

$$\mathcal{L}_{\mathrm{HE}} = \mathcal{L}_{\mathrm{M}} + \mathcal{L}_{\mathrm{HE}}^{\text{1-loop}}\,, \tag{2.2}$$

where $\mathcal{L}_{\mathrm{M}}$ is the Maxwell Lagrangian and $\mathcal{L}_{\mathrm{HE}}^{\text{1-loop}}$ the 1-loop correction. Expressing this as an effective action is done by

$$\Gamma_{\mathrm{HE}} = \int \mathrm{d}^4x\, \mathcal{L}_{\mathrm{HE}}\,, \tag{2.3}$$

the Heisenberg-Euler effective action. The well known Maxwell Lagrangian can be written in several ways

$$\mathcal{L}_{\mathrm{M}} = -\mathcal{F} = -\frac{1}{4}F^{\mu\nu}F_{\mu\nu} = -\frac{1}{2}\left(\boldsymbol{B}^2 - \boldsymbol{E}^2\right)\,, \tag{2.4}$$

with electric field $\boldsymbol{E}$, magnetic field $\boldsymbol{B}$, and the components of the field strength tensor $F^{\mu\nu}$ describing the classical background EM field. Additionally, we introduce two relativistic invariants $\mathcal{F}$ and $\mathcal{G}$ of the field strength tensor given by

$$\mathcal{F} = \frac{1}{4}F_{\mu\nu}F^{\mu\nu} = \frac{1}{2}\left(\boldsymbol{B}^2 - \boldsymbol{E}^2\right) \quad \text{and} \quad \mathcal{G} = \frac{1}{4}F_{\mu\nu}\tilde{F}^{\mu\nu} = -\boldsymbol{B}\cdot\boldsymbol{E}\,, \tag{2.5}$$

where $\tilde{F}^{\mu\nu} = \frac{1}{2}\varepsilon_{\mu\nu\alpha\beta}F^{\alpha\beta}$ is the Hodge dual field strength tensor. As metric convention we choose $g_{\mu\nu} = \mathrm{diag}(-1,+1,+1,+1)$. Keeping the Euler-Lagrange equations in mind, it is directly apparent that the equations of motion (EOM) for ED are linear, because $\mathcal{L}_\mathrm{M}$ is quadratic in the fields. The 1-loop effective Lagrangian can be written as [15]

$$\mathcal{L}_\mathrm{HE}^\text{1-loop} = -\frac{1}{8\pi^2}\int_0^\infty \frac{\mathrm{d}T}{T^3}\mathrm{e}^{-m_e^2 T}\left[\frac{(eaT)(ebT)}{\tan(eaT)\tanh(ebT)} + \frac{1}{3}(eT)^2\left(a^2-b^2\right) - 1\right], \tag{2.6}$$

with secular invariants

$$a = \left(\sqrt{\mathcal{F}^2+\mathcal{G}^2}-\mathcal{F}\right)^{1/2} \quad \text{and} \quad b = \left(\sqrt{\mathcal{F}^2+\mathcal{G}^2}+\mathcal{F}\right)^{1/2}. \tag{2.7}$$

Note that (2.6) differs slightly from the version given by Heisenberg and Euler in [12], as they used the CGS system of units. We use the Heaviside-Lorentz system with $c = \hbar = 1$ for the theoretical background given in section 2 and SI units in the numerical calculations of sections 3 and 4. Equation (2.6) is only valid for external EM fields $F^{\mu\nu}$ that vary slowly compared to the reduced Compton wavelength and time of the electron. In fact, the derivation of (2.6) assumes the external EM field to be homogeneous. This restriction is later loosened using a *locally constant field approximation* (LCFA); see [14, 63]. This is a well justified approximation, as the spatial and temporal extend of quantum fluctuations is on the order of the reduced Compton wavelength $\lambda\!\!\!^{-}_\mathrm{C} \approx 3.86\times10^{-13}\,\mathrm{m}$ and time $\tau_\mathrm{C} \approx 1.29\times10^{-21}\,\mathrm{s}$. Both quantities are much smaller than the scale of variation of inhomogeneous EM fields in experiment. We can therefore treat the external background fields as locally constant for the purpose of quantum vacuum fluctuation mediated nonlinear couplings between them. The EM fields available in experiment also justify treating the background as classical in (2.1), because quantum effects can be neglected for the produced field strengths and length scales.

The diagrammatic representation of the 1-loop Heisenberg-Euler effective action is given by

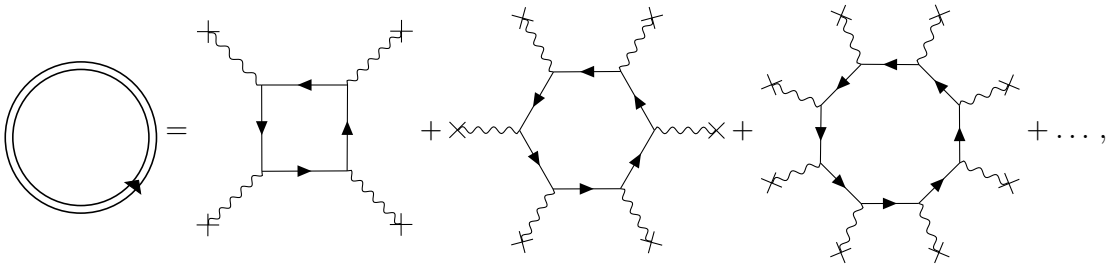

(2.8)

where the double line represents the dressed fermion propagator

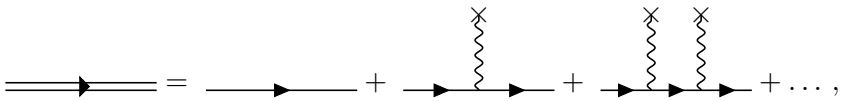

(2.9)

and $\times$ marks external legs. Note that the number of vertices is always even in accordance with Furry's theorem [64].

To solve the integral in (2.6), we make use of a weak-field expansion with expansion parameter $\epsilon \sim \frac{ea}{m_e^2} \sim \frac{eb}{m_e^2}$. The leading order $\mathcal{O}(\epsilon^4)$ result is given by [15]

$$\mathcal{L}_{\mathrm{HE}}^{\text{1-loop}} \approx \frac{m_e^4}{360\pi^2}\left(\frac{e}{m_e^2}\right)^4\left(a^4+5a^2b^2+b^4\right) = \frac{\alpha}{90\pi}\frac{4\mathcal{F}^2+7\mathcal{G}^2}{E_{\mathrm{cr}}^2}\,, \tag{2.10}$$

where $\alpha = \mathrm{e}^2/(4\pi)$ is the fine structure constant and $E_{\mathrm{cr}} = \frac{m_e^2c^3}{e\hbar} \approx 1.32\times10^{18}\,\mathrm{V/m}$ is the critical electric field strength (Schwinger limit) [65, 66]. (Similarly, one can express a critical magnetic field strength by $B_{\mathrm{cr}} = E_{\mathrm{cr}}/c \approx 4.41\times10^9\,\mathrm{T}$.) For fields approaching the Schwinger limit, higher-order nonlinearities become important. An experimental verification of this theoretical prediction poses a challenge, since state-of-the-art high-intensity (optical) laser facilities generate peak field strengths on the order of $10^{15}\,\mathrm{V/m}$; see [67] for a comparison of facilities.

The 1-loop Heisenberg-Euler effective Lagrangian $\mathcal{L}_{\mathrm{HE}}^{\text{1-loop}}$ is of order α. Neglecting higher loop orders is justified, as they need at least one additional internal photon line and are therefore suppressed by powers of $\alpha \approx 1/137$ [14]. A study past 1-loop order can be found in [63]. The restriction to order $\mathcal{O}(\epsilon^4)$ is a restriction to the four legged diagram of (2.8).

Due to the experimental challenges, a lot of theoretical work is invested into the possibilities of observing the leading nonlinear effects in the weak-field regime. The vacuum emission process provides an efficient framework for these studies.

2.2 Vacuum emission process

The idea of the vacuum emission process, which we describe using Karbstein's VEP [58], is to introduce (quantum) scattering amplitude techniques applied to the Heisenberg-Euler effective action. The process of interest is the nonlinear interaction of (classical) external fields in the vacuum via virtual electron-positron pairs from the quantum fluctuations to create one (quantum) photon. The photon's existence is then a signature of the quantum vacuum nonlinearities, as this process is impossible on the tree level (ED). We use the term "signal" for photons created through the vacuum emission process, and we use the term "background" for the external EM fields.

In current experiment proposals, the background typically dominates the signal on the order of 10^{20} photons. Nevertheless, it might be possible to separate the signal from the background by the properties of the photons and thus enable the detection of nonlinear effects below the Schwinger limit.

In the study of the vacuum emission process, we focus on the transition amplitude from the vacuum (with classical background EM fields) to the one (quantum) photon state. The transition amplitude is given by

$$\mathcal{S}_{(p)}(\boldsymbol{k}) = \left\langle \gamma_\beta(\boldsymbol{k}) \left| \Gamma_{\mathrm{HE}}^{\text{1-loop}} \right| 0 \right\rangle , \tag{2.11}$$

where $\langle \gamma_\beta(\boldsymbol{k})|$ is the one photon state with polarization $\beta \in [0, 2\pi)$ and wave vector $\boldsymbol{k}$, $\Gamma_{\mathrm{HE}}^{\text{1-loop}} = \int \mathrm{d}^4x \; \mathcal{L}_{\mathrm{HE}}^{\text{1-loop}}$ is the interaction term, and $|0\rangle$ denotes the vacuum state. To separately account for background and signal, we decompose the field strength tensor $F^{\mu\nu} \to F^{\mu\nu} + f^{\mu\nu}$, where $F^{\mu\nu}$ is now the classical field strength tensor of the background and $f^{\mu\nu}$ the operator-valued field strength tensor of the signal. The interaction term is then given by the Taylor expansion of the 1-loop Heisenberg-Euler effective action in weak-field expansion (2.10) around the background $F^{\mu\nu}$

$$\mathcal{L}_{\mathrm{HE}}^{\text{1-loop}} = f^{\mu\nu} \frac{\partial \mathcal{L}_{\mathrm{HE}}^{\text{1-loop}}}{\partial F^{\mu\nu}} + \mathcal{O}(f^2) . \tag{2.12}$$

Order $\mathcal{O}(f^2)$, where $f = f^{\mu\nu}$, does not contribute to the process creating one signal photon. Processes creating more than one signal photon are typically suppressed [15]. Using the weak-field expansion result in (2.10) the transition amplitude from vacuum to the one photon state can be written as [40, 67]

$$\begin{aligned} \mathcal{S}_\beta(\boldsymbol{k}) = \frac{1}{\mathrm{i}} \frac{e}{4\pi^2} \frac{m_e^2}{45} \sqrt{\frac{\mathrm{k}}{2}} \left(\frac{e}{m_e^2} \right)^3 \int \mathrm{d}^4x \; \mathrm{e}^{\mathrm{i}kx} \Big[& 4 \left(\boldsymbol{e}_\beta(\boldsymbol{k}) \cdot \boldsymbol{E}(x) - \boldsymbol{e}_{\beta+\frac{\pi}{2}}(\boldsymbol{k}) \cdot \boldsymbol{B}(x) \right) \mathcal{F}(x) \\ & + 7 \left(\boldsymbol{e}_\beta(\boldsymbol{k}) \cdot \boldsymbol{B}(x) - \boldsymbol{e}_{\beta+\frac{\pi}{2}}(\boldsymbol{k}) \cdot \boldsymbol{E}(x) \right) \mathcal{G}(x) \Big] , \end{aligned} \tag{2.13}$$

with wave number $\mathrm{k} = k^0 = |\boldsymbol{k}|$, orthogonal polarization vectors $\boldsymbol{e}_\beta(\boldsymbol{k})$, $\boldsymbol{e}_{\beta+\frac{\pi}{2}}(\boldsymbol{k})$, and $kx = k^\mu x_\mu$. Here, $\{\boldsymbol{e}_\beta(\boldsymbol{k}), \boldsymbol{e}_{\beta+\frac{\pi}{2}}(\boldsymbol{k}), \boldsymbol{e}_{\boldsymbol{k}}(\boldsymbol{k})\}$ forms an orthonormal basis for all β, where $\boldsymbol{e}_{\boldsymbol{k}}(\boldsymbol{k}) = \boldsymbol{k}/\mathrm{k}$. The Feynman diagram for this process

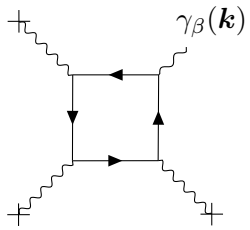

(2.14)

features three external photon legs denoting the coupling to the background and one (quantum) photon leg; *cf.* (2.8). Using the transition amplitude we can gain insight into the vacuum emission process by calculating the signal photon number density

$$\frac{\mathrm{d}^3 N_\beta(\boldsymbol{k})}{\mathrm{d}^3\mathrm{k}} = \frac{1}{(2\pi)^3} \left| \mathcal{S}_\beta(\boldsymbol{k}) \right|^2 , \tag{2.15}$$

where $\mathrm{d}^3\mathrm{k} = \mathrm{k}^2 \, \mathrm{dk} \; \mathrm{d}\Omega$ and $\mathrm{d}\Omega = \sin(\vartheta) \, \mathrm{d}\vartheta \; \mathrm{d}\varphi$. We also refer to (2.15) as the signal spectrum.

2.3 Light-by-light scattering

The process of vacuum emission described in section 2.2 and based on the Heisenberg-Euler effective action (section 2.1) can be interpreted using different pictures. We can interpret the process as photons being emitted from the vacuum, which is subject to macroscopic EM fields. Here, we see the vacuum as the medium in which the EM fields propagate. Its nonlinear properties cause photon emission. There is no need to resolve the microscopic photon structure of the EM fields. Alternatively, we can interpret the process as the scattering of external photon, which creates the signal photon. [58]

Intuitively, the first picture corresponds well to the mathematical treatment above (*e.g.* (2.13)), whereas the second picture captures the microscopic process represented in the Feynman diagram (2.14).

In line with the experimental possibilities, we have already introduced the weak-field expansion in (2.10). Now we want to take into account how the background EM fields are generated. Modern experiments commonly plan to use lasers. They allow for high intensities using ultra short pulses. Note that $\mathcal{F}$ and $\mathcal{G}$ (2.5) vanish for plane waves, because of $\boldsymbol{B} = \boldsymbol{e}_{\boldsymbol{k}}(\boldsymbol{k}) \times \boldsymbol{E}$. The same is true for Gaussian beams in zeroth order paraxial approximation. And as $\mathcal{F} = \mathcal{G} = 0$ leads to a vanishing signal amplitude $\mathcal{S}_\beta$, this motivates using more than one laser to attain nonvanishing invariants [58]. It is, of course, not the only way, but it additionally has the advantage of increasing the field strength in the interaction area. For an analytical study of an n-lasers configuration, see [67]. Experimentally, it is difficult to focus the lasers to one spacetime point. Therefore, we restrict ourselves to using exactly two lasers. In this case, we have two laser angular frequencies ω_1 and ω_2. Using (2.14) and conservation of energy, we find the possible signal angular frequencies ω to be [40]

$$\begin{aligned} \omega \in \{&\omega_1,\, \omega_1 + 2\omega_2,\, |\omega_1 - 2\omega_2|,\\ &\omega_2,\, \omega_2 + 2\omega_1,\, |\omega_2 - 2\omega_1|\}\,. \end{aligned} \tag{2.16}$$

Trivially, we see that for $\omega_1 = \omega_2 = \omega_0$ the possible signal photon angular frequencies reduce to

$$\omega \in \{\omega_0,\, 3\omega_0\}\,. \tag{2.17}$$

This is an idealization, as the energy spectrum of Gaussian beams is smeared out. Nevertheless, (2.16) and (2.17) tell us where the signal peaks in the energy spectrum.

3 Numerical simulation of the vacuum emission process

In general, it is not possible to find a closed-form expression for the signal amplitude (2.13). There are special cases that allow for analytical study, oftentimes making use of the infinite Rayleigh range approximation; *e.g.* [59]. Numerically solving the signal amplitude opens up a wide range of new regimes. Based on the VEP a numerical simulation code was developed by Blinne in 2019 [61]. We refer to it by the name "VacEm code". The VacEm code is written in `Python` and makes use of optimized libraries to achieve high performance.

Section 3 uses SI units, since the code should produce results giving direct orientation for future experiments. We start by understanding the inner workings of the VacEm code (section 3.1), then analyze its limitations (section 3.2), and develop improvements (section 3.3).

3.1 VacEm code

The one and only task of the VacEm code is solving the signal amplitude $\mathcal{S}_\beta$ (2.13) given (at least) the background EM fields in the focus. Apart from the input, all calculations are done in the $\boldsymbol{k}$ space.

We examine what the code actually computes (section 3.1.1), how its algorithm works and what this means for memory usage (section 3.1.2), and look at the underlying class structure leading to different possible workflows (section 3.1.3).

3.1.1 Numerical accessibility of the signal amplitude

We now establish how the signal amplitude can be rewritten into an efficient numerically accessible form. The focus here is on the efficiency. The numerical accessibility of (2.13) is already given, as it is only comprised of dot products and a four-dimensional integration. It is possible to rewrite the equations into a form needing fewer operations and making use of fast Fourier transforms (FFT). This section together with the algorithm provided in section 3.1.2 forms the necessary foundation for understanding the capabilities, limitations, and possible improvements of the VacEm code. The following content is based on unpublished notes written by Blinne, combined with direct insights into the source code. (For those with access to the `vacem` repository, see `doc/vacem.pdf`.)

We take the signal amplitude (2.13)

$$\begin{aligned}\mathcal{S}_\beta(\boldsymbol{k}) = \mathcal{A} \int \mathrm{d}^4x\, \mathrm{e}^{\mathrm{i}kx} \Big[&4 \left(\boldsymbol{e}_\beta(\boldsymbol{k}) \cdot \boldsymbol{E}(x) - \boldsymbol{e}_{\beta+\frac{\pi}{2}}(\boldsymbol{k}) \cdot \boldsymbol{B}(x) \right) \mathcal{F}(x) \\ &+7 \left(\boldsymbol{e}_\beta(\boldsymbol{k}) \cdot \boldsymbol{B}(x) - \boldsymbol{e}_{\beta+\frac{\pi}{2}}(\boldsymbol{k}) \cdot \boldsymbol{E}(x) \right) \mathcal{G}(x) \Big]\end{aligned} \tag{3.1}$$

as a starting point, where the prefactor $\mathcal{A}$ is given by

$$\mathcal{A} = \frac{1}{\mathrm{i}} \frac{e}{4\pi^2} \frac{m_e^2}{45} \sqrt{\frac{\mathrm{k}}{2}} \left(\frac{e}{m_e^2} \right)^3 . \tag{3.2}$$

We have normalized the electric field $\boldsymbol{E}$ with the speed of light c to allow for easier notation because now $\boldsymbol{E}$ and $\boldsymbol{B}$ have the same dimension. Instead of grouping the terms by $\mathcal{F}$ and $\mathcal{G}$ we group them by $\boldsymbol{e}_\beta(\boldsymbol{k})$ and $\boldsymbol{e}_{\beta+\frac{\pi}{2}}(\boldsymbol{k})$ to get

$$\begin{aligned} \mathcal{S}_\beta(\boldsymbol{k}) = \mathcal{A} \int \mathrm{d}^4 x \, \mathrm{e}^{\mathrm{i}kx} \big[& \boldsymbol{e}_\beta(\boldsymbol{k}) \cdot (4\boldsymbol{E}(x)\mathcal{F}(x) + 7\boldsymbol{B}(x)\mathcal{G}(x)) \\ & + \boldsymbol{e}_{\beta+\frac{\pi}{2}}(\boldsymbol{k}) \cdot (-\boldsymbol{B}(x)\mathcal{F}(x) + 7\boldsymbol{E}(x)\mathcal{G}(x)) \big] . \end{aligned} \tag{3.3}$$

The unit vector $\boldsymbol{e}_\beta$ is perpendicular to the wave vector

$$\boldsymbol{k} = \begin{pmatrix} k \sin(\vartheta) \cos(\varphi) \\ k \sin(\vartheta) \sin(\varphi) \\ k \cos(\vartheta) \end{pmatrix} , \tag{3.4}$$

where k, ϑ, φ are the spherical coordinates of the $\boldsymbol{k}$ space, and can be parametrized by

$$\boldsymbol{e}_\beta(\boldsymbol{k}) = \begin{pmatrix} \cos(\beta) \cos(\vartheta) \cos(\varphi) - \sin(\beta) \sin(\varphi) \\ \cos(\beta) \cos(\vartheta) \sin(\varphi) - \sin(\beta) \cos(\varphi) \\ -\cos(\beta) \sin(\vartheta) \end{pmatrix} . \tag{3.5}$$

It can also be decomposed as

$$\boldsymbol{e}_\beta(\boldsymbol{k}) = \sin(\beta) \underbrace{\begin{pmatrix} -\sin(\varphi) \\ \cos(\varphi) \\ 0 \end{pmatrix}}_{=\boldsymbol{e}_1(\boldsymbol{k})} + \cos(\beta) \underbrace{\begin{pmatrix} \cos(\vartheta) \cos(\varphi) \\ \cos(\vartheta) \sin(\varphi) \\ -\sin(\vartheta) \end{pmatrix}}_{=\boldsymbol{e}_2(\boldsymbol{k})} . \tag{3.6}$$

Attention: this notation violates standard conventions. To obtain a right-handed basis $\{\boldsymbol{e}_1(\boldsymbol{k})$, $\boldsymbol{e}_2(\boldsymbol{k})$, $\boldsymbol{e}_{\boldsymbol{k}}(\boldsymbol{k})\}$ the labels in (3.6) should be swapped $\boldsymbol{e}_1(\boldsymbol{k}) \leftrightarrow \boldsymbol{e}_2(\boldsymbol{k})$. The VacEm code, and therefore also this section, uses the left-handed basis for an unknown reason. The unit vectors $\boldsymbol{e}_1(\boldsymbol{k})$ and $\boldsymbol{e}_2(\boldsymbol{k})$ can alternatively be expressed in terms of the components of the wave vector $\boldsymbol{k}$ by

$$\boldsymbol{e}_1(\boldsymbol{k}) = \frac{1}{\mathrm{k}_\perp} \begin{pmatrix} -k_y \\ k_x \\ 0 \end{pmatrix} \quad \text{and} \quad \boldsymbol{e}_2(\boldsymbol{k}) = \frac{1}{\mathrm{k}\mathrm{k}_\perp} \begin{pmatrix} k_x k_z \\ k_y k_z \\ -\mathrm{k}_\perp^2 \end{pmatrix} , \tag{3.7}$$

where $\mathrm{k}_\perp = \sqrt{k_x^2 + k_y^2}$. In short, we have

$$\boldsymbol{e}_\beta(\boldsymbol{k}) = \sin(\beta)\boldsymbol{e}_1(\boldsymbol{k}) + \cos(\beta)\boldsymbol{e}_2(\boldsymbol{k}) \quad \text{and} \quad \boldsymbol{e}_{\beta+\frac{\pi}{2}}(\boldsymbol{k}) = \cos(\beta)\boldsymbol{e}_1(\boldsymbol{k}) - \sin(\beta)\boldsymbol{e}_2(\boldsymbol{k}) , \tag{3.8}$$

because $\cos(\beta+\frac{\pi}{2}) = -\sin(\beta)$ and $\sin(\beta+\frac{\pi}{2}) = \cos(\beta)$. Again we regroup the signal photon amplitude, now with respect to $\cos(\beta)$ and $\sin(\beta)$, to get

$$\begin{aligned}\mathcal{S}_\beta(\boldsymbol{k}) = \mathcal{A}\int \mathrm{d}^4x\, \mathrm{e}^{\mathrm{i}kx}\big[&\sin(\beta)\,(\boldsymbol{e}_1(\boldsymbol{k})\cdot(4\boldsymbol{E}\mathcal{F}+7\boldsymbol{B}\mathcal{G}) - \boldsymbol{e}_2(\boldsymbol{k})\cdot(-4\boldsymbol{B}\mathcal{F}+7\boldsymbol{E}\mathcal{G}))\\ &+\cos(\beta)\,(\boldsymbol{e}_2(\boldsymbol{k})\cdot(4\boldsymbol{E}\mathcal{F}+7\boldsymbol{B}\mathcal{G}) + \boldsymbol{e}_1(\boldsymbol{k})\cdot(-4\boldsymbol{B}\mathcal{F}+7\boldsymbol{E}\mathcal{G}))\big]\,.\end{aligned} \tag{3.9}$$

This expression can be split into

$$\mathcal{S}_\mathrm{a}(\boldsymbol{k}) = \int \mathrm{d}^4x\, \mathrm{e}^{\mathrm{i}kx}\big[\boldsymbol{e}_1(\boldsymbol{k})\cdot(4\boldsymbol{E}\mathcal{F}+7\boldsymbol{B}\mathcal{G}) - \boldsymbol{e}_2(\boldsymbol{k})\cdot(-4\boldsymbol{B}\mathcal{F}+7\boldsymbol{E}\mathcal{G})\big]\,, \tag{3.10a}$$

$$\mathcal{S}_\mathrm{b}(\boldsymbol{k}) = \int \mathrm{d}^4x\, \mathrm{e}^{\mathrm{i}kx}\big[\boldsymbol{e}_2(\boldsymbol{k})\cdot(4\boldsymbol{E}\mathcal{F}+7\boldsymbol{B}\mathcal{G}) + \boldsymbol{e}_1(\boldsymbol{k})\cdot(-4\boldsymbol{B}\mathcal{F}+7\boldsymbol{E}\mathcal{G})\big]\,, \tag{3.10b}$$

such that

$$\mathcal{S}_\beta(\boldsymbol{k}) = \mathcal{A}\big(\sin(\beta)\mathcal{S}_\mathrm{a}(\boldsymbol{k}) + \cos(\beta)\mathcal{S}_\mathrm{b}(\boldsymbol{k})\big)\,. \tag{3.11}$$

The VacEm code computes the two signal amplitudes in (3.10) and returns them as its output. Further reformulations are made to achieve high computing efficiency. Looking at (3.10), we see that the expressions

$$\boldsymbol{Q} = 4\boldsymbol{E}\mathcal{F}+7\boldsymbol{B}\mathcal{G}\,, \tag{3.12a}$$

$$\boldsymbol{R} = -4\boldsymbol{B}\mathcal{F}+7\boldsymbol{E}\mathcal{G} \tag{3.12b}$$

both appear twice in (3.10). We use (2.5) to express $\mathcal{F}$ and $\mathcal{G}$ by $\boldsymbol{E}$, $\boldsymbol{B}$. With the newly introduced vectors $\boldsymbol{Q}$, $\boldsymbol{R}$, we write $\mathcal{S}_\mathrm{a}(\boldsymbol{k})$ (analogously for $\mathcal{S}_\mathrm{b}(\boldsymbol{k})$) as

$$\begin{aligned}\mathcal{S}_\mathrm{a}(\boldsymbol{k}) &= \int \mathrm{d}^4x\, \mathrm{e}^{\mathrm{i}kx}\big[\boldsymbol{e}_1(\boldsymbol{k})\cdot\boldsymbol{Q}(x) - \boldsymbol{e}_2(\boldsymbol{k})\cdot\boldsymbol{R}(x)\big]\\ &= \int \mathrm{d}t\, \mathrm{e}^{\mathrm{i}ckt}\int \mathrm{d}^3x\, \mathrm{e}^{-\mathrm{i}\boldsymbol{k}\cdot\boldsymbol{x}}\big[\boldsymbol{e}_1(\boldsymbol{k})\cdot\boldsymbol{Q}(t,\boldsymbol{x}) - \boldsymbol{e}_2(\boldsymbol{k})\cdot\boldsymbol{R}(t,\boldsymbol{x})\big]\\ &= \int \mathrm{d}t\, \mathrm{e}^{\mathrm{i}ckt}\Big[\boldsymbol{e}_1(\boldsymbol{k})\cdot\hat{\boldsymbol{Q}}(t,\boldsymbol{k}) - \boldsymbol{e}_2(\boldsymbol{k})\cdot\hat{\boldsymbol{R}}(t,\boldsymbol{k})\Big]\,,\end{aligned} \tag{3.13}$$

where $\hat{\boldsymbol{Q}}(t,\boldsymbol{k})$ and $\hat{\boldsymbol{R}}(t,\boldsymbol{k})$ are the (spatial) Fourier transforms given by

$$\hat{\boldsymbol{Q}}(t,\boldsymbol{k}) = \int \mathrm{d}^3x\, \mathrm{e}^{-\mathrm{i}\boldsymbol{k}\cdot\boldsymbol{x}}\boldsymbol{Q}(t,\boldsymbol{x}) \quad\text{and}\quad \hat{\boldsymbol{R}}(t,\boldsymbol{k}) = \int \mathrm{d}^3x\, \mathrm{e}^{-\mathrm{i}\boldsymbol{k}\cdot\boldsymbol{x}}\boldsymbol{R}(t,\boldsymbol{x})\,. \tag{3.14}$$

Attention: in (3.13) we have used the metric convention $g_{\mu\nu} = \mathrm{diag}(+1,-1,-1,-1)$ in contrast to the theoretical background section 2. This is done to yield the conventional Fourier transform from position to $\boldsymbol{k}$ space with factor $e^{-\mathrm{i}\boldsymbol{k}\cdot\boldsymbol{x}}$. Of course, it does not have impact on the scalar signal amplitude. We end up with

$$\mathcal{S}_\mathrm{a}(\boldsymbol{k}) = \int \mathrm{d}t\, \mathrm{e}^{\mathrm{i}ckt}\Big[\boldsymbol{e}_1(\boldsymbol{k})\cdot\hat{\boldsymbol{Q}}(t,\boldsymbol{k}) - \boldsymbol{e}_2(\boldsymbol{k})\cdot\hat{\boldsymbol{R}}(t,\boldsymbol{k})\Big]\,, \tag{3.15a}$$

$$\mathcal{S}_\mathrm{b}(\boldsymbol{k}) = \int \mathrm{d}t\, \mathrm{e}^{\mathrm{i}ckt} \left[\boldsymbol{e}_2(\boldsymbol{k}) \cdot \hat{\boldsymbol{Q}}(t,\boldsymbol{k}) + \boldsymbol{e}_1(\boldsymbol{k}) \cdot \hat{\boldsymbol{R}}(t,\boldsymbol{k})\right] , \tag{3.15b}$$

the two parts of the signal photon amplitude in a form accessible to efficient numerical calculation. As input to the calculation, we need the $\boldsymbol{E}$ and $\boldsymbol{B}$ fields as functions of spacetime. The VacEm code supports two options for the so called `fieldmode`: "explicit" and "solver". As the names suggest, this gives us the choice between defining the fields as analytical functions of spacetime or provide initial data at the focus and propagate it by solving the Maxwell equations in vacuum. The field propagation is done using the Maxwell solver put forward in [68].

The above equations are sufficient to understand the inner workings of the VacEm code for `fieldmode = 'explicit'`. When using `fieldmode = 'solver'` some additional calculations are required to propagate the focus input data to all required times. Up to this point, we worked with real electric and magnetic fields. Due to the Maxwell solver getting employed in the VacEm code, we now need to treat the electric and magnetic fields as complex. This makes a substitution of $\boldsymbol{E} \to \Re(\boldsymbol{E})$ and $\boldsymbol{B} \to \Re(\boldsymbol{B})$ in all earlier equations necessary.

In `fieldmode = 'solver'` the code makes use of complex spectral amplitudes $a_{0p}(\boldsymbol{k})$. They get introduced with the electromagnetic potential in radiation gauge, where $A^\mu = (0, \boldsymbol{A})$ and $\boldsymbol{\nabla} \cdot \boldsymbol{A} = 0$. We write the electromagnetic potential using its Fourier transform

$$\boldsymbol{A}(t,\boldsymbol{x}) = \int \frac{\mathrm{d}^3\mathrm{k}}{(2\pi)^3} \mathrm{e}^{\mathrm{i}\boldsymbol{k}\cdot\boldsymbol{x}} \hat{\boldsymbol{A}}(t,\boldsymbol{k}) , \tag{3.16}$$

and define the complex spectral amplitudes $a_{0p}(\boldsymbol{k})$ (amplitudes in the two orthogonal polarization directions) through

$$\hat{\boldsymbol{A}}(t,\boldsymbol{k}) = \mathrm{e}^{-\mathrm{i}ckt} \sum_{p=1}^{2} \boldsymbol{e}_p(\boldsymbol{k}) a_{0p}(\boldsymbol{k}) . \tag{3.17}$$

Any possible choice for the spectral amplitudes leads to a solution of the Maxwell equations. This also allows for easy time propagation of the EM fields. It only requires a simple multiplication of the spectral amplitudes for each wave vector $\boldsymbol{k}$ with the corresponding temporal phase term $\exp(-\mathrm{i}ckt)$. For $\boldsymbol{E}$ and $\boldsymbol{B}$ (Remember, the electric field is normalized by c.) we find

$$\boldsymbol{E}(t,\boldsymbol{x}) = -\frac{\partial_t \boldsymbol{A}(t,\boldsymbol{x})}{c} = \int \frac{\mathrm{d}^3\mathrm{k}}{(2\pi)^3} \sum_{p=1}^{2} \mathrm{i}\mathrm{k} a_{0p}(\boldsymbol{k}) \boldsymbol{e}_p(\boldsymbol{k}) \mathrm{e}^{\mathrm{i}(\boldsymbol{k}\cdot\boldsymbol{x} - ckt)} , \tag{3.18a}$$

$$\boldsymbol{B}(t,\boldsymbol{x}) = \boldsymbol{\nabla} \times \boldsymbol{A}(t,\boldsymbol{x}) = \int \frac{\mathrm{d}^3\mathrm{k}}{(2\pi)^3} \sum_{p=1}^{2} a_{0p}(\boldsymbol{k}) \boldsymbol{\nabla} \times \boldsymbol{e}_p(\boldsymbol{k}) \mathrm{e}^{\mathrm{i}(\boldsymbol{k}\cdot\boldsymbol{x} - ckt)} . \tag{3.18b}$$

The cross products turn out to be

$$\boldsymbol{\nabla} \times \boldsymbol{e}_1(\boldsymbol{k}) \mathrm{e}^{\mathrm{i}\boldsymbol{k}\cdot\boldsymbol{x}} = -\mathrm{i}\mathrm{k} \boldsymbol{e}_2(\boldsymbol{k}) \mathrm{e}^{\mathrm{i}\boldsymbol{k}\cdot\boldsymbol{x}} \quad \text{and} \quad \boldsymbol{\nabla} \times \boldsymbol{e}_2(\boldsymbol{k}) \mathrm{e}^{\mathrm{i}\boldsymbol{k}\cdot\boldsymbol{x}} = \mathrm{i}\mathrm{k} \boldsymbol{e}_1(\boldsymbol{k}) \mathrm{e}^{\mathrm{i}\boldsymbol{k}\cdot\boldsymbol{x}} . \tag{3.19}$$

Therefore, the Fourier transforms of the $\boldsymbol{E}$ and $\boldsymbol{B}$ fields can be written as

$$\hat{\boldsymbol{E}}(t,\boldsymbol{k}) = \mathrm{ik}\left[\boldsymbol{e}_1(\boldsymbol{k})a_1(t,\boldsymbol{k}) + \boldsymbol{e}_2(\boldsymbol{k})a_2(t,\boldsymbol{k})\right], \tag{3.20a}$$

$$\hat{\boldsymbol{B}}(t,\boldsymbol{k}) = \mathrm{ik}\left[\boldsymbol{e}_1(\boldsymbol{k})a_2(t,\boldsymbol{k}) - \boldsymbol{e}_2(\boldsymbol{k})a_1(t,\boldsymbol{k})\right], \tag{3.20b}$$

where

$$a_p(t,\boldsymbol{k}) = \mathrm{e}^{-ickt}a_{0p}(\boldsymbol{k}), \tag{3.21}$$

and we have

$$\boldsymbol{E}(t,\boldsymbol{x}) = \int \frac{\mathrm{d}^3\mathrm{k}}{(2\pi)^3}\mathrm{e}^{\mathrm{i}\boldsymbol{k}\cdot\boldsymbol{x}}\hat{\boldsymbol{E}}(t,\boldsymbol{k}) \quad \text{and} \quad \boldsymbol{B}(t,\boldsymbol{x}) = \int \frac{\mathrm{d}^3\mathrm{k}}{(2\pi)^3}\mathrm{e}^{\mathrm{i}\boldsymbol{k}\cdot\boldsymbol{x}}\hat{\boldsymbol{B}}(t,\boldsymbol{k}). \tag{3.22}$$

To obtain the complex spectral amplitudes we use

$$a_{0p}(\boldsymbol{k}) = \mathrm{e}^{\mathrm{ik}t_0}\frac{1}{\mathrm{ik}}\boldsymbol{e}_p(\boldsymbol{k})\cdot\hat{\boldsymbol{E}}(t_0,\boldsymbol{k}). \tag{3.23}$$

See Blinne [61] for different methods, as this choice is not unique. We note that the complex spectral amplitudes can also be used to write down an expression for the background photon number density (in analogy to (2.15)) as

$$\frac{\mathrm{d}^3\mathcal{N}(\boldsymbol{k})}{\mathrm{d}^3\mathrm{k}} = \frac{\varepsilon_0 c\mathrm{k}}{2\hbar}\left(|a_{01}(\boldsymbol{k})|^2 + |a_{02}(\boldsymbol{k})|^2\right), \tag{3.24}$$

where ε_0 is the vacuum permittivity. We now have all the necessary equations in place for the VacEm code.

3.1.2 Algorithm and memory usage

Let us review the workings of the code by studying its pseudocode algorithm in listing 1.

Listing 1: VacEm code algorithm in pseudocode for `fieldmode = 'solver'`.

```
INPUT config.ini (+ complex128 E fields focus data)
a_01, a_02 ⟵ FieldSolver.from_config('config.ini').a0
S_a, S_b ⟵ 0
FOR each time t from t_start to t_stop with step of size Δt
    a_1, a_2 ⟵ eq.(3.21)(a_01, a_02)
    Ê_i, B̂_i ⟵ eq.(3.20)(a_1, a_2)
    E_i, B_i ⟵ iFFT_3(Ê_i, B̂_i)
    F, G ⟵ eq.(2.5)(E_i, B_i)
    Q_i ⟵ eq.(3.12a)(E_i, B_i, F, G)
```

10 $\hat{Q}_i \longleftarrow \mathrm{FFT}_3(Q_i)$

11 $\mathcal{S}_\mathrm{a} \longleftarrow \mathcal{S}_\mathrm{a} + \mathrm{e}^{\mathrm{i}ckt}\boldsymbol{e}_1 \cdot \hat{\boldsymbol{Q}}$

12 $\mathcal{S}_\mathrm{b} \longleftarrow \mathcal{S}_\mathrm{b} + \mathrm{e}^{\mathrm{i}ckt}\boldsymbol{e}_2 \cdot \hat{\boldsymbol{Q}}$

13 $R_i \longleftarrow$ `eq.(3.12b)`$(E_i, B_i, \mathcal{F}, \mathcal{G})$

14 $\hat{R}_i \longleftarrow \mathrm{FFT}_3(R_i)$

15 $\mathcal{S}_\mathrm{a} \longleftarrow \mathcal{S}_\mathrm{a} - \mathrm{e}^{\mathrm{i}ckt}\boldsymbol{e}_2 \cdot \hat{\boldsymbol{R}}$

16 $\mathcal{S}_\mathrm{b} \longleftarrow \mathcal{S}_\mathrm{b} + \mathrm{e}^{\mathrm{i}ckt}\boldsymbol{e}_1 \cdot \hat{\boldsymbol{R}}$

17 `ENDFOR`

18 $\mathcal{S}_\mathrm{a} \longleftarrow \mathcal{S}_\mathrm{a}\Delta t$

19 $\mathcal{S}_\mathrm{b} \longleftarrow \mathcal{S}_\mathrm{b}\Delta t$

20 `OUTPUT ndarray complex128` $\mathcal{S}_\mathrm{a}, \mathcal{S}_\mathrm{b}$

Listing 1 gives the pseudocode for `fieldmode = 'solver'`. For `fieldmode = 'explicit'` lines {2, 5, 6, 7} are neglected, as $\boldsymbol{E}$, $\boldsymbol{B}$ are known explicitly. The abbreviation FFT_3 denotes the three-dimensional fast Fourier transform and iFFT_3 its inverse. We see that the time integration from (3.15) is done using the rectangle rule (left Riemann sum). This might seem oddly simple but is a justified choice, since the error introduced by the time integration is expected to be much smaller than the overall error of the result.

The generated result file contains $\mathcal{S}_\mathrm{a}$, $\mathcal{S}_\mathrm{b}$ together with some additional data concerning debugging and performance; see section 3.1.3. With the pseudocode at hand, we can think about the memory usage (RAM) of the VacEm code. Of course, there is also the concern of data storage, but it is not a limiting factor in our case. The input is given in terms of a configuration file in the `.ini` format; see listing 2. It is a short text file of negligible size. In addition to the simulation volume (L_x, L_y, L_z) and grid (N_x, N_y, N_z), the `.ini` file either contains the parameters of the lasers (*e.g.* pulsed Gaussian beams) or the path to stored complex $\boldsymbol{E}$ field profile data; see section 3.1.3 for further explanations. The latter case typically requires several tens of gigabytes (GB) of data storage for the input. The same is true for the output data. Let us return to the far more important question of memory usage. In lines 2, 3 the complex spectral amplitudes and the signal amplitudes get initialized. The complex spectral amplitudes are instances of the `postpic.Field` class. The signal amplitudes are instances of the `numpy.ndarray` class, *i.e.* `NumPy` arrays. `Postpic` is a post-processor for particle-in-cell simulations co-developed by Blinne [69]. Instances of the `Field` class are made up of a matrix and axes. For fields of three-dimensional space the matrix is naturally also three-dimensional and therefore its memory requirements ($\propto N_x \times N_y \times N_z$) exceed those of the three one-dimensional axes ($\propto (N_x + N_y + N_z)$).

For this reason we only focus on the matrix part. This means that for our memory analysis the `postpic.Field` is equivalent to the `numpy.ndarray`. The memory allocated for a field (*i.e.* the matrix representing the field) is given by its size $N_x \times N_y \times N_z$ and the data type of each matrix element. We are working with floating-point numbers (floats), which take up 64 bit as the default in `Python`. They are commonly called double-precision floats to separate them from single-precision floats with 32 bit. More on the topic can be found in section 3.3.2. Complex numbers have a real and an imaginary part, both described by 64 bit-floats, and take up 128 bit. They are represented using the `complex128` data type. One complex field therefore allocates $N_x \times N_y \times N_z \times 128\,\mathrm{bit}$. (Keep in mind that $8\,\mathrm{bit} = 1\,\mathrm{byte}$.) The four complex fields initialized for input and output in lines 2, 3 define the lower limit of memory usage. For usability reasons, we have to know the maximum required memory for a given simulation. We need to know the maximum number of fields allocated at the same time and their data type. The algorithm is implemented in such a way that FFT/iFFT is always done in-place. The same idea for reducing memory usage is applied to $\boldsymbol{Q}$ and $\boldsymbol{R}$, as they are only needed once per loop and never together. Listing 1 shows that complex fields a_{01}, a_{02}, $\mathcal{S}_\mathrm{a}$, $\mathcal{S}_\mathrm{b}$, a_1, a_2, $\boldsymbol{E}$, $\boldsymbol{B}$, $\boldsymbol{Q}$ and real fields $\mathcal{F}$, $\mathcal{G}$, $\boldsymbol{e}_1\,\boldsymbol{e}_2$ or their respective replacements are allocated at the same time. The resulting memory usage $\mathrm{RAM}_\mathrm{min}$ is given by

$$\mathrm{RAM}_\mathrm{min} = N_x N_y N_z (15 \times 128\,\mathrm{bit} + 8 \times 64\,\mathrm{bit}) \frac{10^{-9}\,\mathrm{GB}}{8\,\mathrm{bit}}\,, \tag{3.25}$$

where vectors count as 3. As part of the configuration `.ini` file, we have the parameter `low_memory_mode` with default value `False`. It leads to better performance and additionally accumulates $\mathcal{S}_{a/b,d}$ for $d \in 2, 4$ only taking into account every d-th time step. The latter part allows for a convergence test of the time integration but requires four more complex fields. Of course, there are also temporary allocations affecting the peak memory usage. While performing simulations with the VacEm code it became apparent that we obtain a good estimate for the peak memory usage by

$$\mathrm{RAM}_\mathrm{peak} = \frac{4}{3} N_x N_y N_z \times 23 \times 128\,\mathrm{bit} \frac{10^{-9}\,\mathrm{GB}}{8\,\mathrm{bit}}\,. \tag{3.26}$$

With this analysis of the memory usage, we have found one of the main problems of the VacEm code. A three-dimensional grid with hundreds or thousands of grid points in each direction easily leads to severe memory requirements. Looking at tab. 1 the problem becomes obvious.

Table 1: Memory usage for different grid sizes.

$N_x N_y N_z$	$\mathrm{RAM}_{\mathrm{min}}$ in GB	$\mathrm{RAM}_{\mathrm{peak}}$ in GB
$128 \times 128 \times 128$	1	1
$256 \times 256 \times 256$	5	8
$512 \times 512 \times 512$	41	66
$1024 \times 1024 \times 1024$	326	527
$2048 \times 2048 \times 2048$	2611	4215
$4096 \times 4096 \times 4096$	20 891	33 718

Already at $1024 \times 1024 \times 1024$ grid points, we exceed the available memory per node on a typical HPC-cluster, and $4096 \times 4096 \times 4096$ approaches the technical limit in available memory on one node for any currently available system. (The state-of-the-art "big memory" HPC *Mammoth* of *Lawrence Livermore National Laboratory* features 2 TB of memory per node [70].) Note that the VacEm code implementation is only made to run on one node; see section 3.3.1. Our choice of $N_x = N_y = N_z = 2^n$ in tab. 1 is not necessary, we provide more details on this matter in section 3.2.2.

The question remains which number of grid points is needed to resolve the laser pulses and their interaction. This depends on the temporal and spatial frequencies involved. The details are provided in section 3.2.2. In general, the complexity of the systems of interest exceeds the available memory resources even at HPC-clusters like *Draco* [62]. Special cases allow for generating new insights using reasonable hardware resources. Of course, Blinne did already think about these problems. He wrote:

> "[...] our code is capable of calculating signal photon emission amplitudes in completely generic input field configurations, limited only by numerical cost." (Blinne 2019 [71])

In addition to the memory usage, the time complexity is also an important part of the numerical cost. We do not analyze the time complexity of the VacEm code in this work. Nevertheless, the time it takes to finish one simulation is important. It is later discussed in section 3.3.1.

We conclude this section with the remark that the memory usage, or in general the numerical cost, is indeed the only limiting factor (section 3.2) of the VacEm code in simulating the zero-to-one signal photon transition amplitude for the process represented in (2.14).

3.1.3 Class structure and workflow

From the pseudocode algorithm (section 3.1.2), we move on to the actual structure of the VacEm code. The class structure forms the core of the `Python` implementation. Understanding it is necessary for operating and improving the code. We analyzed and visualized the class structure using the tools `pyreverse` from `pylint` [72] in combination with `graphviz` [73]. The diagrammatic representation of the class structure of the VacEm code can be seen in fig. 1. (Classes for testing purposes are excluded.)

Figure 1: Class structure of the VacEm code.

In fig. 1 each box represents a class. Classes belonging to the same package have the same color. The arrows show the class inheritance, pointing from the child class to the parent class. We see three "families" here, all yellow boxes. `GridSpecification` and `SolverBase` are used to define the simulation box and grid in position and $\boldsymbol{k}$ space. Additionally, they carry some useful properties of the simulation. `SpectralSolution`, `ExplicitSolution`, `ComplexEInput`, `GaussianParaxial`, and `GaussianSpectral` handle the EM fields (lasers) input. The classes `AbstractSolver`, `ExplicitFields` and `FieldSolver` take care of providing the EM field data at each time step. `VacEm` contains all methods required for the different lines of the algorithm (listing 1). The class `ResultFile` allows for easy evaluation of the results. Figure 1 shows the provided data attributes and methods for each class.

Different workflows are possible with the given class structure. Let us start with the input. The input creates an instance of one of the three classes `GaussianParaxial`, `GaussianSpectral`, or `ComplexEInput`. Each of these classes allows for different EM field profiles. `GaussianParaxial`, as the name suggests, is used to initialize a pulsed Gaussian beam (3.27) with the parameters

in tab. 2.

Table 2: Parameters of the `GaussianParaxial` class.

Symbol	Variable	Name
λ	`lambda`	wavelength
w_0	`w0`	beam waist
τ	`tau`	pulse duration
$\mathcal{E}_0$	`E0`	peak field amplitude
ϕ_0	`phi0`	phase shift
$\mathcal{O}((w_0/z_\mathrm{R})^n)$	`order`	order of paraxial approximation
β	`beta`	roll (pulse polarization)
ϑ	`theta`	pitch (pulse orientation)
φ	`phi`	yaw (pulse orientation)
t_focus	`focus_t`	focus time
$\boldsymbol{x}_\mathrm{focus}$	`focus_x`	focus position

The quantity $z_R = \pi w_0^2/\lambda$ is the Rayleigh range of the pulse. The default for `focus_t` and `focus_x` is given by `0.0` and `(0.0, 0.0, 0.0)`. It is the same for all three classes and a very useful choice in the "middle" of the simulation volume and time frame. Note that the simulation volume axes are defined by $[[-L_x/2, L_x/2], [-L_y/2, L_y/2], [-L_z/2, L_z/2]]$ and the time frame by $[-L_t/2, L_t/2]$. We leave the focus at the center of our simulation spacetime throughout this work. Nevertheless, there also exist interesting possibilities by shifting the focus of one of the pulses; see [27]. The Euler angles `beta, theta, phi` are defined such that `(0.0, 0.0, 0.0)` describes pulse propagation in $+z$ direction with polarization vector in $+x$ direction. The `order` parameter defines the order of paraxial approximation. The Gaussian beam is a solution of the paraxial Helmholtz equation. It relies on the paraxial approximation, which is a slowly varying envelope approximation. It is justified for beams that are not strongly divergent, *i.e.* divergence $w_0/z_\mathrm{R} \ll 1$. This does not hold in general; *e.g.* in cases of tight focusing. We are therefore interested in higher order corrections, *i.e.* an expansion in orders of w_0/z_R. See [74] for the derivation up to order 11. Order 1 corresponds to the "standard" Gaussian beam. Order 0 gives us the infinite Rayleigh range approximation, *i.e.* $z_R \to \infty$. The VacEm code enables the usage of `order` `0` to `5`. The parameters w_0, τ mark by the intensity drop-off to $1/e^2$, not full width at half maximum (FWHM). This is again a standard for the VacEm code.

We already introduced the `fieldmode` parameter in section 3.1.1, which gives us the choice between providing the EM fields explicitly (`'explicit'`) and propagating the EM fields from the focus using the Maxwell solver (`'solver'`). Since `GaussianParaxial` is based on a closed-form expression for the EM field as a function of the point in spacetime, it supports both `'explicit'` and `'solver'` `fieldmode`. (If you know the field at each time, then you also know it at the focus time.)

We ignore the class `GaussianSpectral`. It is designed for a specialized use case that we are not interested in. See [61, section D.2] [75] for an explanation of this class.

The most powerful input class, and the class of interest for us, is `ComplexEInput`. It allows to provide an arbitrary complex $\boldsymbol{E}$ field at t_{focus} as a `postpic.Field`. In this case, we do not know the $\boldsymbol{E}$ field each simulation time step, which limits us to the usage of `fieldmode = 'solver'`. The parameters of `ComplexEInput` are shown in tab. 3.

Table 3: Parameters of the `ComplexEInput` class.

Symbol	Variable	Name
E_x, E_y, E_z	`Ex, Ey, Ez`	complex electric field input components (active or stored `postpic.Field` instance)
β_{input}	`input_beta`	input coordinates roll (pulse polarization)
ϑ_{input}	`input_theta`	input coordinates pitch (pulse orientation)
φ_{input}	`input_phi`	input coordinates yaw (pulse orientation)
β	`beta`	roll (pulse polarization)
ϑ	`theta`	pitch (pulse orientation)
φ	`phi`	yaw (pulse orientation)
$\boldsymbol{x}_{\text{input\_center}}$	`input_center`	center of input coordinates
t_{focus}	`focus_t`	focus time (time of input data)
$\boldsymbol{x}_{\text{focus}}$	`focus_x`	focus position
λ_{input}	`lambda`	wavelength when only providing envelope

The set of parameters allows for a very convenient way of providing input data. The field components `Ex, Ey, Ez` may be generated from an analytical expression or another simulation software. In both cases, one might be restricted to the use of a certain propagation direction and polarization. This is no problem, because one can provide the roll, pitch, yaw of the pulse in the input coordinate system to `ComplexEInput`. The class takes care of rotating the pulse

inversely to the "neutral" position and then rotates it into the desired direction and polarization (`beta, theta, phi`). With `input_center` we set the point around which the rotation should be executed. The `lambda` parameter can be used when only inputting the envelope instead of the electric field.

The current state of VacEm therefore allows for three types of input:

- pulsed Gaussian beams (`'explicit'`)
- pulsed Gaussian beams (`'solver'`)
- arbitrary complex EM fields (`'solver'`)

Furthermore, the VacEm code can simulate systems combining multiple and possibly different input types. Let us examine what that looks like in practice. We provide an example `.ini` file in listing 2 that is later used in section 4.

Listing 2: `ComplexEInput` example configuration of the system in fig. 13 (section 4).

```
[Setup]
N = 675, 675, 675
L = 7.12936756395725e-05, 7.12936756395725e-05, 7.12936756395725e-05
lasers = 2
low_memory_mode = False
float_precision = single
[Run]
t_start = -1.1890505204032268e-13
t_end = 1.1890505204032268e-13
t_steps = 672
fieldmode = solver
[laser_1]
type = complex_e_input
focus_x = 0.0, 0.0, 0.0
focus_t = 0.0
input_center = 0, 0, 0
theta = 90.0
phi = 90.0
beta = 180.0
```

```
input_theta = 90.0
input_phi = -90.0
input_beta = 90.0
Ex = cpftves_pt_7_E0_hole.npz
[laser_2]
type = complex_e_input
focus_x = 0.0, 0.0, 0.0
focus_t = 0.0
input_center = 0, 0, 0
theta = 90.0
phi = -90.0
beta = 180.0
input_theta = 90.0
input_phi = -90.0
input_beta = 90.0
Ex = cpftves_pt_7_006_E0.npz
```

Most of the parameters shown in listing 2 have already been explained. What remains is the `lasers` parameter. The VacEm code can simulate systems with an arbitrary number of lasers. The laser `type` is independent, *i.e.* we can *e.g.* simulate a system with one laser described using the `GaussianParaxial` class and one by `ComplexEInput`. The `type` parameter has the options `gaussian_paraxial`, `gaussian_spectral`, `complex_e_input` as keywords for the respective classes. For fast creation of configuration files, we created multiple scripts (one for each `type`). Their code is loosely based on work by Blinne.

This concludes the input part of the workflow with the VacEm code. To actually run the code a script `vacem_solver.py` is provided. The execution command is given by

```
vacem_solver.py load_ini {jobname}.ini
```

where `{jobname}` is a placeholder for the name of the `.ini` file. There exist of course more options for `vacem_solver.py`. Using the conventional

```
vacem_solver.py ---help
```

they can be printed to the terminal. After a simulation has finished a result file `{jobname}_vacem.npz` is saved. The `NumPy .npz` file format is a zip file containing multiple `NumPy .npy`

files. A `.npy` file holds the complete information of one `NumPy` array. The content of the result file is shown in listing 3.

Listing 3: Content of a VacEm code result file (`low_memory_mode = False`).

```
s1 (2, Nx, Ny, Nz)
s2 (2, Nx, Ny, Nz)
s4 (2, Nx, Ny, Nz)
grid (3,)
kgrid (3,)
t (t_steps,)
nrg_input_fields_spatial ()
nrg_input_fields ()
performance ()
```

Each line in listing 3 is a `NumPy` array with the shape shown in brackets. The shape `()` belongs to scalars. The main result is given by `s1`. It contains the signal amplitudes $\mathcal{S}_a$, $\mathcal{S}_b$. The additional accumulators $\mathcal{S}_{a/b,d}$ for every second ($d = 2$) or every forth time step ($d = 4$) are saved as `s2` and `s4`. (Remember, they are only accumulated if `low_memory_mode = False`.) Note that in the result file the prefactor $\mathcal{A}$ (3.2) is not yet applied. Fortunately, there is no need to work directly with the result file. The class `ResultFile` is built for convenient evaluation of the result files. It provides methods that apply the correct prefactor to the signal amplitudes, calculates the total signal spectrum or the signal spectrum for a given polarization (2.15).

As a last step, we want to include the visualization of the signal spectrum into the workflow. The signal spectrum is a three-dimensional `postpic.Field`. For visualization purposes it is therefore best to reduce its dimension by at least one. Reducing the dimensionality can either be done through slicing or integration. Both dimensionality reduction and visualization can be tedious and require hundreds of code lines. To accelerate and simplify this process we have created the `vacem_plot` function. It completely automates the visualization process. Oftentimes, we want to convert the result from Cartesian to spherical coordinates. A mapping function doing this operation is already provided as part of the VacEm code (`field_to_spherical`). Note that this mapping naturally introduces a small error. Further explanations follow in section 3.2.1. There we also show plots obtained with our plotting function `vacem_plot`.

3.2 Limitations

Section 3.1 and [61, 71] show the broad capabilities of the VacEm code in simulating the vacuum emission process. As already stated, it is only limited by numerical cost. In this section, we analyze the consequences of working with a finite volume and grid. Based on the theoretical and algorithmic background (section 3.1), we hypothesize that infinite computational resources (and infinite discretization of an infinite volume) would reduce the result error to zero. Our interest lies in determining the needed spacetime volume size and grid point density for obtaining qualitatively correct results with quantitatively small error.

3.2.1 Finite volume

The volume of the simulation box is defined by lengths L_t, L_x, L_y, L_z. Based on (2.13) we would like to work with $L_{t,x,y,z} \to \infty$. Unfortunately, only finite volumes are possible numerically, and the numerical cost grows with the volume size. If the chosen volume is too small, information of the background EM fields is "cut off" and therefore lost. Additionally, small spatial volumes are problematic, because we are employing FFTs of non-periodic functions. It is important to develop a heuristic for large enough L_t, L_x, L_y, L_z as a function of the spatial and temporal envelope of the lasers pulses. We do this based on a pulsed Gaussian beam, but it also gives us baseline parameters for studying more complex beam profiles. We look at propagation in $+z$ direction and polarization in x direction, *w.l.o.g* . The real E_x field for a pulsed Gaussian beam is given by [67]

$$\begin{aligned} E_x(t,\boldsymbol{x}) =& \mathcal{E}_0 \underbrace{\frac{w_0}{w(z)} \exp\left(-\frac{x_\perp^2}{w(z)^2}\right)}_{\text{spatial envelope}} \underbrace{\exp\left(-\frac{4(z/c-t)^2}{\tau^2}\right)}_{\text{temporal envelope}} \\ & \times \underbrace{\cos\left(\mathrm{k}z - \omega t + \mathrm{k}\frac{x_\perp^2}{2R(z)} - \arctan\left(\frac{z}{z_\mathrm{R}}\right) + \phi_0\right)}_{\text{field oscillations}}, \end{aligned} \tag{3.27}$$

with beam radius $w(z) = w_0\sqrt{1+(z/z_R)^2}$, radius of curvature $R(z) = z(1+(z_R/z)^2)$, and distance from the beam axis $x_\perp = \sqrt{x^2+y^2}$. We want to choose the simulation box volume such that the envelope at the boundary drops off to $\leq \xi \times \mathcal{E}_0$ compared to the peak value $\mathcal{E}_0$. We choose the drop-off parameter $\xi = 10\,\%$ as an initial guess. That number might seem rather large. It is justified, because the terms contributing to the signal amplitude (2.13) are always field amplitude to the third power and $(10\,\%)^3 = 0.1\,\%$.

We know that the largest error from the analytical approximations in the VEP is due to the restriction to 1-loop order. 2-loop order is suppressed by the fine-structure constant $\alpha \approx 1/137$.

Therefore, the error of the analytical approximation is on the order of 1 %.
The field oscillations have no importance at this point. Let us assign the label $\mathcal{C}$ to the combined envelope (product of spatial and temporal envelope) and examine the drop-off for different cases to determine the required volume size.

- Case: $t = L_z/(2c)$, $x_\perp = 0$, $z = L_z/2$

$$\begin{aligned} C(t, x_\perp, z) &= \left(1 + \left(\frac{L_z}{2z_\mathrm{R}}\right)^2\right)^{-1/2} \stackrel{!}{=} \xi \\ L_z &= 2z_\mathrm{R}\sqrt{\xi^{-2} - 1} \\ &= \frac{2\pi w_0^2}{\lambda}\sqrt{\xi^{-2} - 1} \end{aligned} \tag{3.28}$$

- Case: $t = L_z/(2c)$, $x_\perp = L_{x_\perp}/2$, $z = z_\mathrm{max}$

$$\begin{aligned} C(t, x_\perp, z) &= \frac{w_0}{w(z_\mathrm{max})} \exp\left(-\frac{L_{x_\perp}^2}{4w(z_\mathrm{max})^2}\right) \stackrel{!}{=} \xi \\ L_{x_\perp} &= \max_z 2w(z)\sqrt{\ln\left(\frac{w_0}{\xi w(z)}\right)} \end{aligned} \tag{3.29}$$

- Case: $t = \tilde{L}_t/2$, $x_\perp = 0$, $z = 0$

$$\begin{aligned} C(t, x_\perp, z) &= \exp\left(-\frac{\tilde{L}_t^2}{\tau^2}\right) \stackrel{!}{=} \xi \\ \tilde{L}_t &= \tau\sqrt{\ln(\xi^{-1})} \\ L_t &= \max(\tilde{L}_t, L_z/c) \end{aligned} \tag{3.30}$$

Note that $L_x = L_y = L_{x_\perp}$, and that for a different propagation direction of the pulse we assign $2w_0\sqrt{\ln(\xi^{-1})}$ to all axes orthogonal to the propagation direction and $\frac{2\pi w_0^2}{\lambda}\sqrt{\xi^{-2} - 1}$ to all other axes.

Unfortunately, the above considerations based on the EM field drop-off are not enough to find good parameters for the volume size. The $\boldsymbol{k}$ space grid point density does also depend on the spatial volume size ($\Delta k_{x,y,z} = L_{x,y,z}^{-1}$ for $N_{x,y,z} \gg 1$). It is nontrivial to develop a criterion for the needed $\Delta k_{x,y,z}$. What we can do is to use the above expressions for $L_{t,x,y,z}$ and see if $\xi = 10\,\%$ leads to a large enough simulation volume or if adjustments have to be made to reduce numerical artifacts. The system we use as an example consists of two lasers, each with $\lambda = 820\,\mathrm{nm}$, $w_0 = 820\,\mathrm{nm}$, $\tau = 41\,\mathrm{fs}$, $W = 244\,\mathrm{J}$. The propagation takes place in the x-y plane ($\vartheta = 90°$), one in the direction $\varphi_1 = 39.6°$ and the other towards $\varphi_2 = 90°$. The polarization angles are given by $\beta_1 = \beta_2 = \pi/4$. We use the `GaussianParaxial` class at `order = 1` and

with `fieldmode = 'explicit'`. The parameters are based on the capabilities of HPLS at ELI-NP [76, 77]. The system is taken from work by Sundqvist [60], as it is well suited for our purpose of identifying numerical artifacts. Note that we use `float_precision = 'single'` for the simulations; see section 3.3.2. With the volume size from (3.28) to (3.30) and $\xi = 10\,\%$, we obtain the background and signal photon number densities displayed in fig. 2. The grid point density we use throughout section 3.2.1 is high enough that we can be certain in attributing appearing numerical artifacts to the finite volume. More details are provided in section 3.2.2.

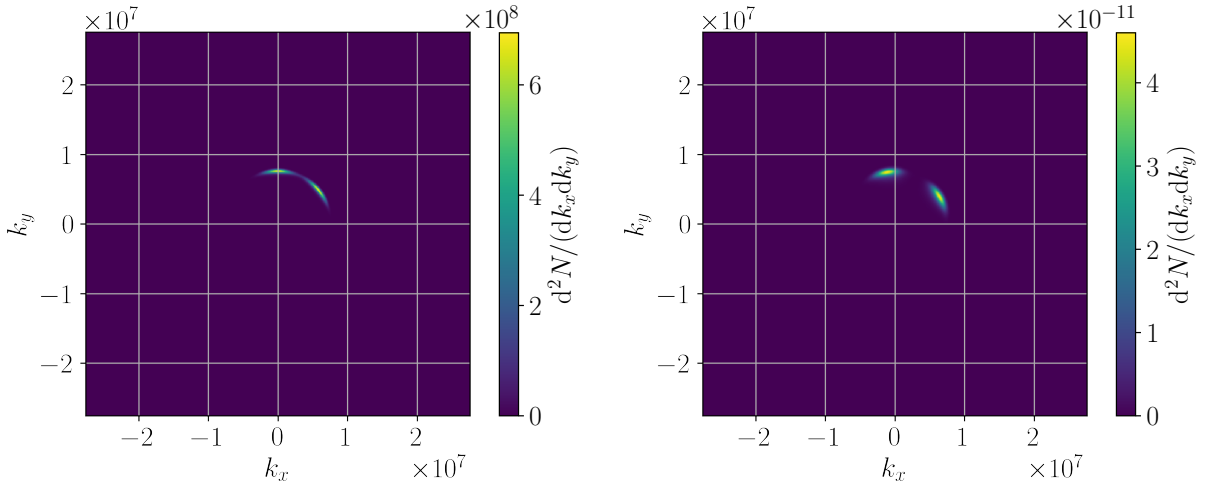

(a) Background (b) Signal

Figure 2: Background and signal photon number densities for our `GaussianParaxial` example system.

Note that N in the color scale labels is the generic placeholder for the total photon number. Figure 2a shows the background photon number density and fig. 2b the signal photon number density. The results are always the sum of both orthogonal polarization directions. Concerning the background photons (fig. 2a), *i.e.* laser photons, we see two local maxima ("spots") corresponding to the two pulsed Gaussian beams. The right one belongs to $\varphi_1 = 39.6°$ and the left one to $\varphi_2 = 39.6°$. The angles of spherical coordinates are identical in position and $\boldsymbol{k}$ space. Both spots have the same distance from $(0, 0)$, as both lasers operate at the same wavelength. The spots are not point-like, since we are working with Gaussian beams, not plane waves. The signal generated through the vacuum emission process (fig. 2b) is 19 orders of magnitude smaller than the background. It resembles the background but is slightly smeared out and shifted.
We do not want to go deep into the physical interpretation of the results. This section focuses on the numerical aspects. To be able to visualize possible artifacts, we study the same plots again

but now with a logarithmic color scale; see fig. 3. The logarithmic scale is cut off at 10 orders of magnitude below the maximum. There is no physical importance of the photon number density at the lower end of the scale, since the analytical approximations in the VEP lead to an accuracy on the order of 1 %. Nevertheless, it is interesting to study how well the VacEm code solves (2.13). Our cut-off choice is, of course, arbitrary but strikes a good balance between including too much detail and not being able to show any numerical artifacts.

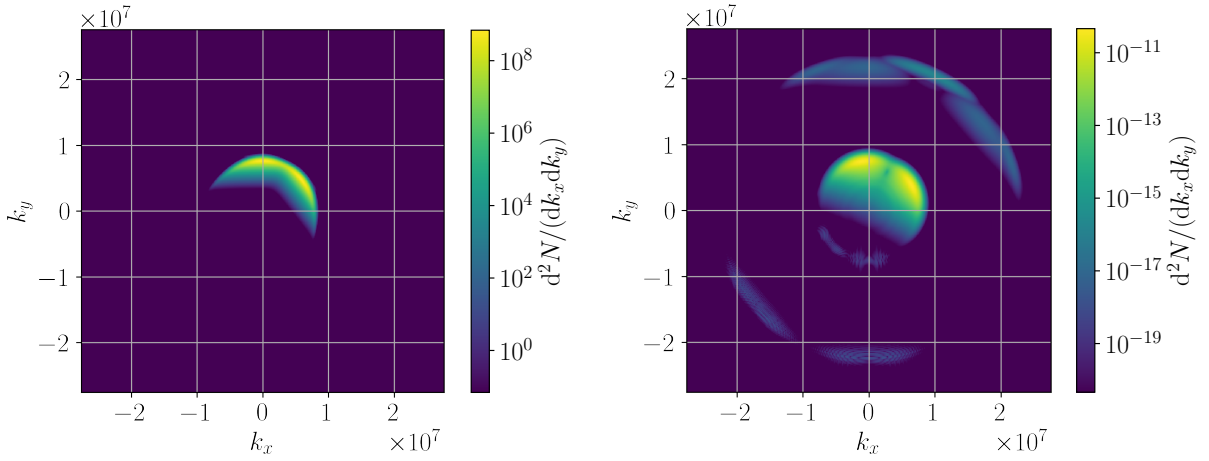

(a) Background (b) Signal

Figure 3: Background and signal photon number densities for our `GaussianParaxial` example system using a logarithmic color scale.

The background photon number density in fig. 3a looks reasonable. Due to the logarithmic scale the spots grown in size. It is interesting to note that the visible fade towards small energies is due to the integration along the k_z axis. It is similar to projecting a part of a sphere (photons of the same energy) onto a plane (x-y plane).

Figure 3b clearly shows false results. The vacuum emission process has to conserve not only energy (2.16) but also momentum. In the lower left quadrant of the plot, we see signal photons generated in the backwards direction and violating conservation of momentum. These effects are indeed later identified as numerical artifacts. They vanish using a larger time interval. One could argue that they are suppressed by roughly 8 orders of magnitude and therefore can be neglected. Nevertheless, we see them as important. They indicate numerical artifacts which makes the overall result questionable, and they are partly on the same order of magnitude as the possibly correct $3\omega_0$ signal in the upper right of the plot.

Talking about the photon energies, visualization using polar plots is useful. As mentioned in section 3.1.3 the VacEm code provides the `field_to_spherical` mapping utility. Polar plots

are easily generated with `vacem_plot` and shown in fig. 4.

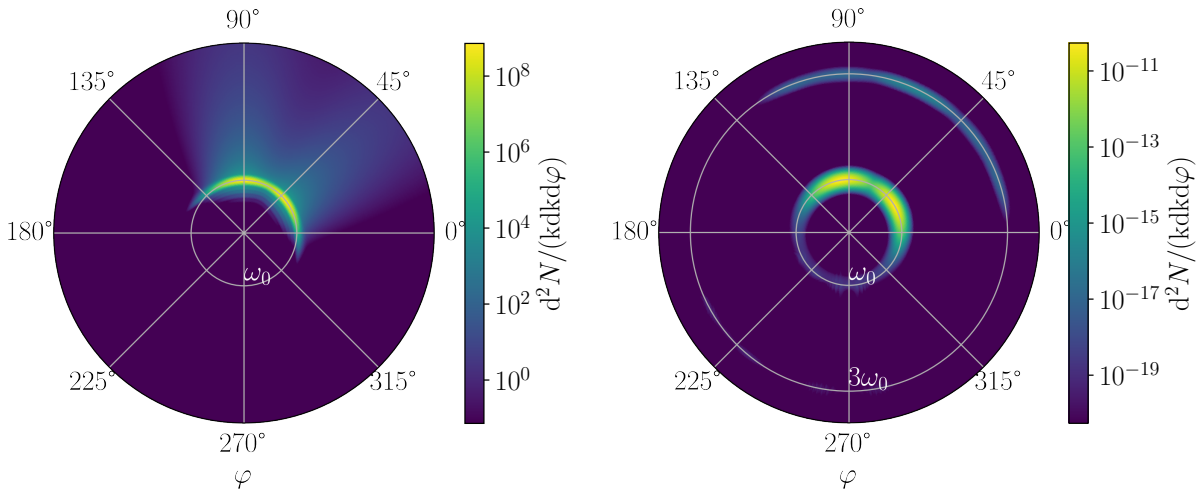

(a) Background (b) Signal

Figure 4: Background and signal photon number densities for our `GaussianParaxial` example system visualized using polar coordinates.

Figure 4 beautifully shows the usefulness of polar plots visualizing the photon number densities. As expected, the background photons (fig. 4a) are concentrated at ω_0, the angular frequency of the lasers. We use the label ω_0, as the two lasers angular frequencies ω_1, ω_2 are equal ($\omega_0 = \omega_1 = \omega_2$). The angular frequency ω_0 should not be confused with the beam waist w_0. (The radial axis actually describes the wave number k, but we use $\omega = c\mathrm{k}$ as labels.) Comparing fig. 3 and 4 we see major differences. There are two things that could be responsible. First, the `field_to_spherical` mapping can cause unwanted effects. The constructed sphere encapsulates the whole input box and has therefore a larger volume, which in turn requires extrapolation. The volume difference is especially strong if one or two edges of the box are significantly smaller than the largest one. In the case at hand, the mapping should not cause relevant artifacts, because the $\boldsymbol{k}$ space box is a cube. We achieved this by using the same grid point density along each position space axis; see section 3.2.2. Second, the data for fig. 3 is integrated over k_z, whereas the data for fig. 4 is integrated over ϑ. Both can be useful depending on the application/experiment. Of course, the energy spectrum in fig. 4a does not correctly describe the example system. The photon number density at high energies is not physical but has to be a numerical artifact. Comparing it to fig. 3a, we know the effect has to stem from the k_z component. Together with the different integration axes, this explains why the effect only becomes visible in fig. 4a. The differences from fig. 3b to fig. 4b are also caused by the different integration axis. The artifacts

at $3\omega_0$ in the backwards direction are still visible even though highly suppressed. The ones at ω_0 have not changed.

Besides the input data cut-off loss we studied at the beginning of this section 3.2.1, there are two possible causes for the numerical artifacts: the FFT and the time integration. All artifacts of the background are caused by the FFT. The background photon number density is calculated by (3.24) based on the complex spectral amplitudes (3.23). Numerical artifacts appear, because the complex spectral amplitudes are proportional to the Fourier transform of the $\boldsymbol{E}$ field. The signal numerical artifacts enter when Fourier transforming $\boldsymbol{Q}$, $\boldsymbol{R}$ (3.12). Both are separate. There is no transfer from the background (input) to the signal, since we are working with `fieldmode = 'explicit'`. Using `fieldmode = 'solver'`, the artifacts from the Fourier transform of the input $\boldsymbol{E}$ fields have direct impact on the signal; see fig. 5.

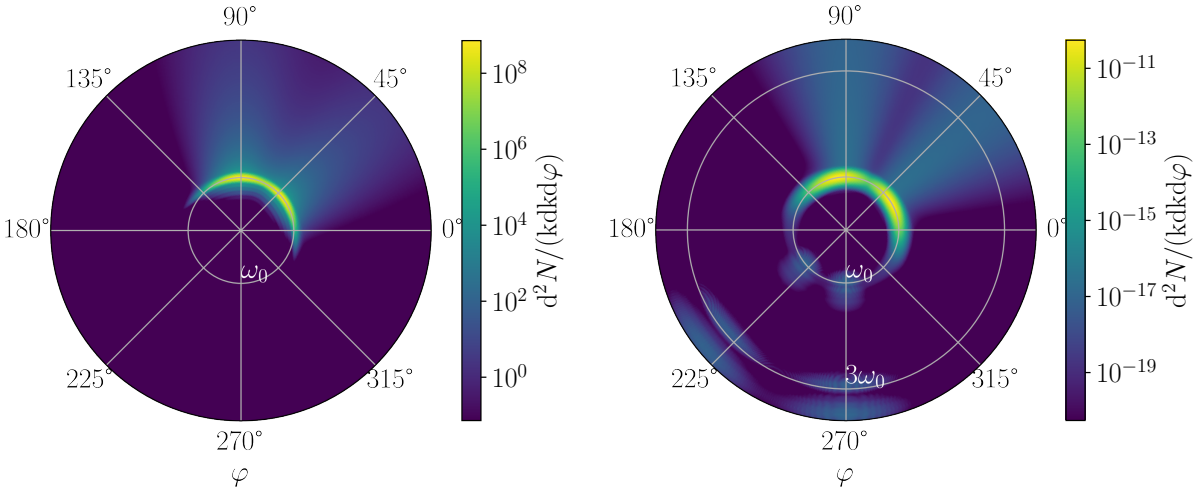

(a) Background (b) Signal

Figure 5: Background and signal photon number densities for our `GaussianParaxial` example system using `fieldmode = 'solver'`.

We revert to using `fieldmode = 'explicit'` for the remainder of section 3.2. Figure 5 shows how numerical artifacts appearing in the background also appear in the signal when using `fieldmode = 'explicit'`. As the overarching goal of this research area is a discernible signal on top of the background, we are interested in reducing artifacts in both background and signal. This brings us back to the question of why the FFT generates the smearing out artifact in fig. 4a. Depending on the function that is Fourier transformed in one dimension, a certain axis length is required to suppress the artifacts. We do not perform a quantitative analysis of the topic here. Just note that the different envelope function in the propagation direction compared to the one

in the orthogonal direction require different axis lengths. The lengths (3.28) and (3.29), derived solely based on the $\boldsymbol{E}$ field drop-off, are large enough in the propagation direction but not in the orthogonal direction. Choosing all spatial dimensions to have the same length, the longest length from (3.28) and (3.29), solves this problem. (This is not the only possible choice. An increase of L_z to a value close to $L_{x,y}$ is needed. Choosing $L_z = L_{x,y}$ is just for convenience.) In fig. 6, we can see that the k_z component actually was the problem and that increasing L_z resolves it. In fig. 7, we see the background and signal photon number densities from fig. 4 again, now with artifact-free background.

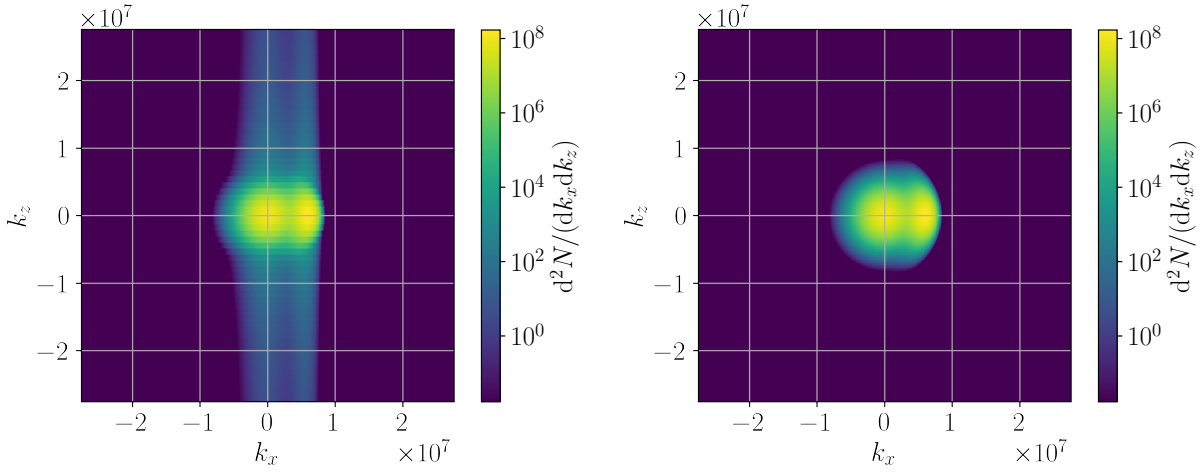

(a) Background, $L_z =$ (3.29)

(b) Background, $L_z = L_{x,y} =$ (3.28)

Figure 6: Background photon number densities for our `GaussianParaxial` example system comparing the influence of L_z.

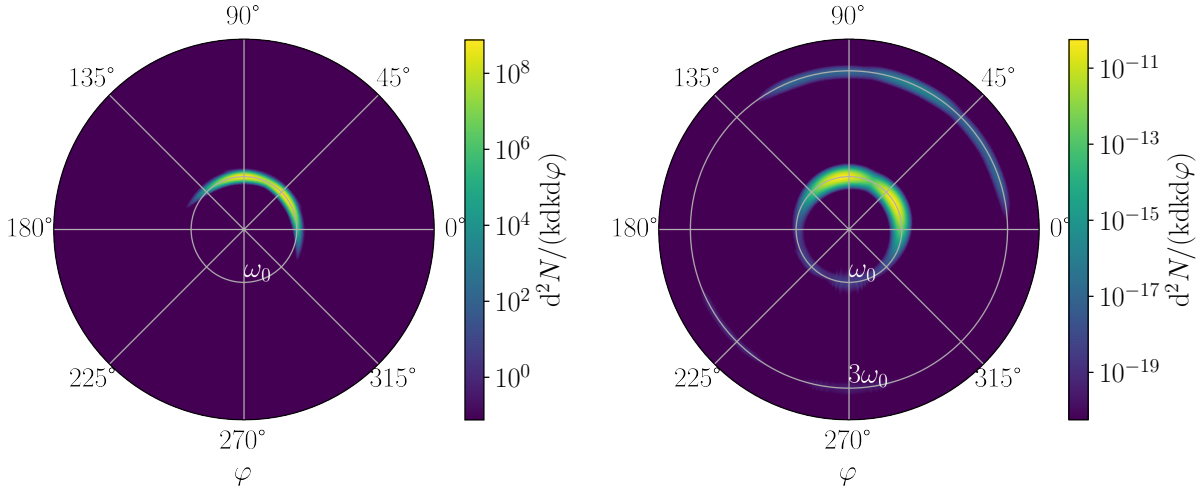

(a) Background (b) Signal

Figure 7: Background and signal photon number densities for our `GaussianParaxial` example system using $L_z = L_{x,y} =$ (3.28).

Even though fig. 7 features an artifact-free background (fig. 7a), the signal remains unchanged (fig. 7b). There is still the (weak) false signal in the background direction. *A priori*, it is impossible to tell if the artifacts are caused by the finite temporal length or spatial volume. Nevertheless, we focus now on the temporal aspect. We do this, because the spatial volume is already approaching the limit of our computational resources. The simulation for the results visualized in fig. 7 had a peak memory usage of roughly 70 GB. Increasing the spatial axis lengths by only a factor of 1.6 would be enough to exceed the available memory of 256 GB.
The time integration only affects the signal. Its computational cost is not memory usage but only computation time. We simulate the above system using a two and three times larger time interval L_t. The obtained signal photon number density is visualized in fig. 8.

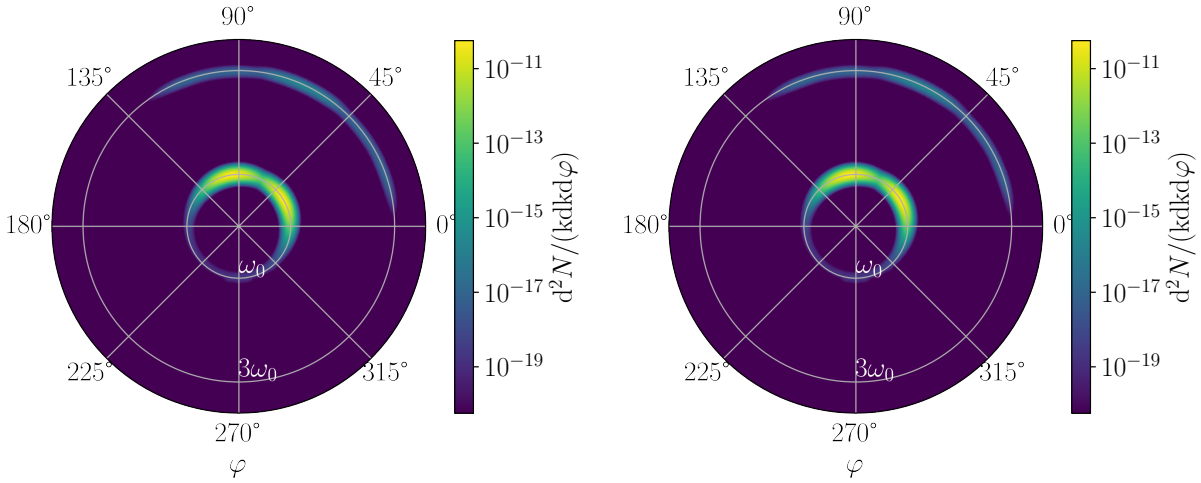

(a) Signal, $2L_t$ (b) Signal, $3L_t$

Figure 8: Signal photon number densities for our `GaussianParaxial` example system for two and three times larger time interval L_t.

Increasing the time interval by a factor of 2 (fig. 8a) eliminates the $3\omega_0$ signal in the backwards direction. The probable explanation lies in the oscillating integrand. Integrating over a finite interval can lead to terms not canceling each other that would do so when integrating from $-\infty$ to ∞. A further increase of the time interval is not justified; see fig. 8b. The false ω_0 signal in the backwards direction is reasonably suppressed but still existent. It is assumed to vanish for an even larger simulation spacetime volume. The remaining $3\omega_0$ signal in the forward direction shows the phenomenon of photon merging.

Now that we found an adequate parameter set ($L_t = 2 \times$ (3.30), $L_{x,y,z} =$ (3.28)), we take a step back and visualize the temporal and spatial finite length/volume numerical artifacts separately. We show the results obtained using only a half or a fourth of the time interval $L_t =$ (3.30) in fig. 9. Similarly, we do a simulation using only a fourth of the spatial axis lengths $L_{x,y,z} =$ (3.28) and plot the background and signal photon number densities in fig. 10.

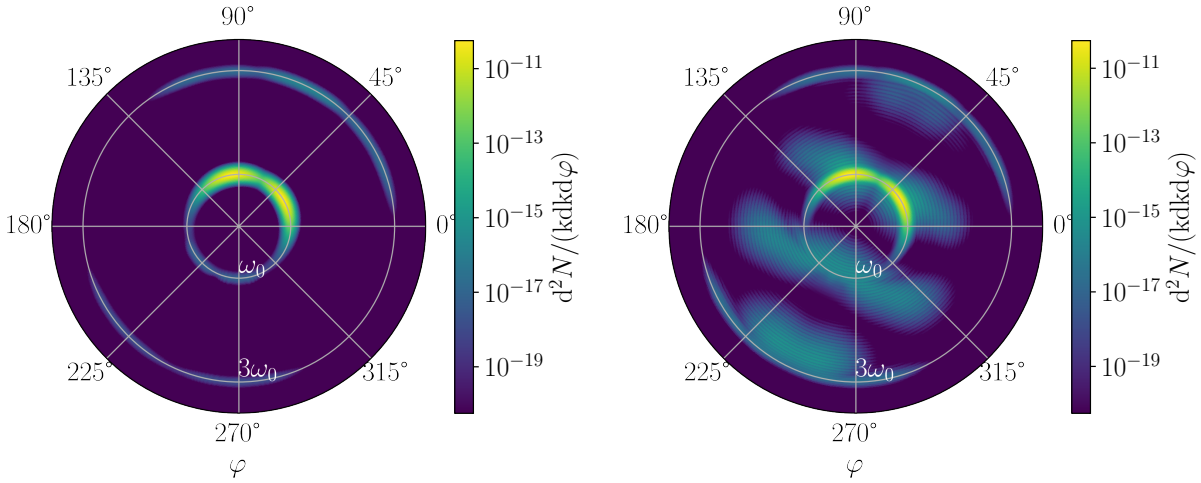

(a) Signal, $L_t = 0.5 \times$ (3.30)

(b) Signal, $L_t = 0.25 \times$ (3.30)

Figure 9: Signal photon number densities for our `GaussianParaxial` example system for a half and a fourth of the time interval L_t.

Figure 9a shows the false $3\omega_0$ signal stronger than before. Using an even shorter time interval (fig. 9b) leads to a characteristic periodic pattern along the symmetry axis between the two laser spots.

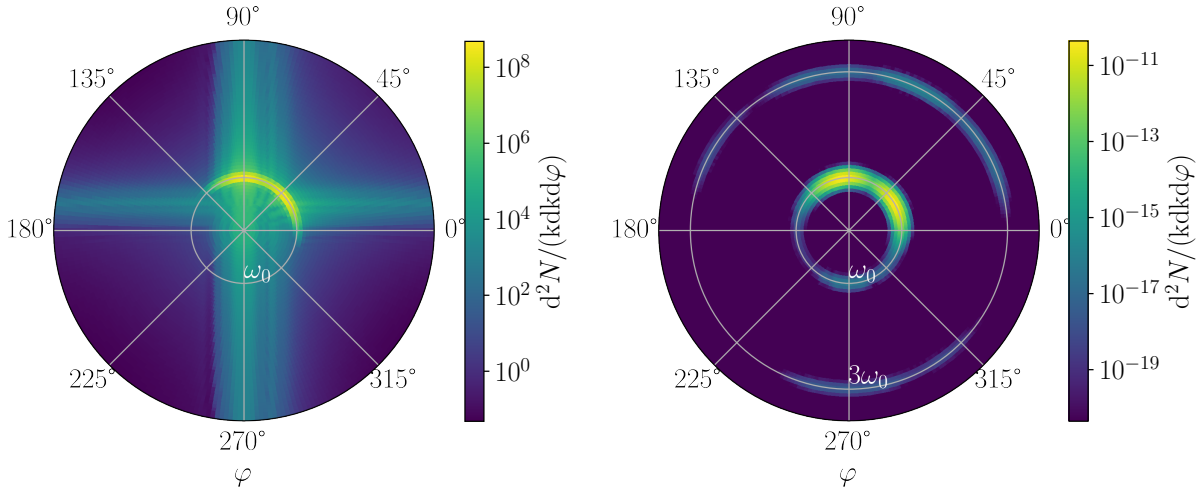

(a) Background, $L_{x,y,z} = 0.25 \times$ (3.28)

(b) Signal, $L_{x,y,z} = 0.25 \times$ (3.28)

Figure 10: Background and signal photon number densities for our `GaussianParaxial` example system for a fourth of the spatial axis lengths $L_{x,y,z}$.

We already know the effect of an insufficiently large spatial volume from fig. 4 to 6. Figure 10 confirms that it leads to a false identification of the wave vector. The photon number density gets

smeared out along the Cartesian $\boldsymbol{k}$ space axes (fig. 10a), which leads to false signals (fig. 10b). Remember that using `fieldmode = 'solver'` would mean that the cross-type artifact from fig. 10a also appears in fig. 10b.

Figures 9 and 10 show that temporal and spatial numerical artifacts caused by insufficient length/volume are nicely distinguishable. This helps us when using `ComplexEInput`, where we can not easily derive a heuristic for the needed simulation spacetime volume.

We have found that with the current computational resources, it is not possible to suppress numerical artifacts to machine precision. It is also not necessary to do so. We have identified different types of numerical artifacts for the VacEm code, and we have shown how it is possible to suppress them in order to obtain physically significant results.

3.2.2 Finite grid point density

In the previous section 3.2.1, we have analyzed the volume-dependent numerical artifacts given a sufficient grid point density. Now we provide the details on how to choose the grid point density to avoid related numerical artifacts without incurring an unreasonably high computational cost. Similar to the volume, the ideal grid point density would be infinitely high. In practice, the grid point density has to be large enough to sufficiently resolves the involved frequencies. For pulsed Gaussian beams this means we need to resolve $\omega_{1,2} = 2\pi c/\lambda_{1,2}$ for the background (input) and (2.16) for the signal. We continue using the example system from section 3.2.1. Therefore, we need to resolve $3\omega_0$. Note that we mean this both temporally and spatially, *i.e.* resolve $3\omega_0$ along the t axis and $3\mathrm{k}_0 = 3\omega_0/c$ along the x, y, z axes. It should be possible to obtain reasonable results with a lower grid point density in the z direction due to the lasers propagating in the x-y plane. Nevertheless, we use the same grid point density for all spatial axes, because this leads to a $\boldsymbol{k}$ space with equal axis lengths. As mentioned in section 3.2.1, this is the desired case when using `field_to_spherical` to evaluate the results in spherical coordinates.

How many grid points are required to resolve a certain frequency? To answer this question, we make use of the *Nyquist-Shannon sampling theorem*. It provides a criterion to avoid aliasing, *i.e.* overlapping of different frequency components.

Theorem. *If a function $f(t)$ contains no frequencies higher than W* cps*, it is completely determined by giving its ordinates at a series of points spaced $1/(2W)$ seconds apart.* [78]

The unit cps is “cycles per second” and is equivalent to Hz. In other words the theorem states that we need at least two points per period/wavelength.

We compare the two cases of using 2.1 or 2.5 points per period/wavelength. For the simulation spacetime volume, we use $L_t = 2 \times$ (3.30), $L_{x,y,z} =$ (3.28) from section 3.2.1. The previous section 3.2.1 used 3.025 points per period/wavelength. The results obtained for 2.1 and 2.5 points per period/wavelength at $3\omega_0$ are visualized in fig. 11.

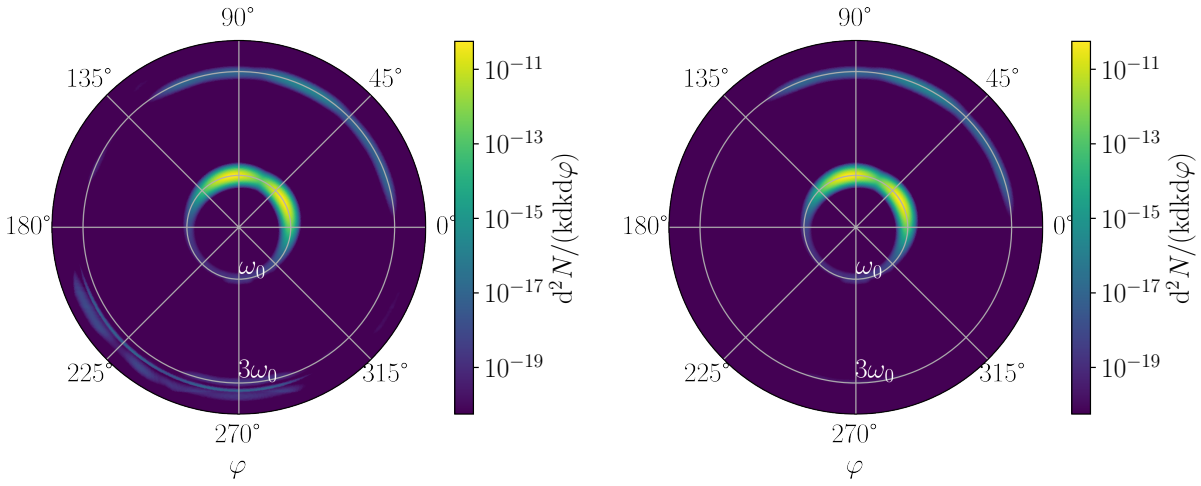

(a) Signal, 2.1 points per period/wavelength at $3\omega_0$ (b) Signal, 2.5 points per period/wavelength at $3\omega_0$

Figure 11: Signal photon number densities for our `GaussianParaxial` example system with different grid point densities.

When studying fig. 11, it is important to realize that the plotting routine `vacem_plot` defaults to cropping the $\boldsymbol{k}$ space at $1.2 \times 3\mathrm{k}_0$. Nevertheless, even for higher wave numbers no numerical artifacts appear in fig. 11b. Hence, there is no significant advantage in using higher grid point densities than fig. 11b; *cf.* fig. 8a. Using 2.1 points per period/wavelength at $3\omega_0$ also fulfills the *Nyquist-Shannon sampling theorem* but is insufficient. Numerical artifacts appear in the lower left quadrant of fig. 11a. This is presumably caused by the fact that the $3\omega_0$ signal is smeared out, since already the pulsed Gaussian beams background is smeared around ω_0. Therefore, the absolute highest frequency that needs to be resolved is slightly above $3\omega_0$, making 2.1 points at $3\omega_0$ inadequate.

One might be only interested in the ω_0 signal. Unfortunately, it is not enough for this to resolve ω_0 and no higher frequencies. We have tested 3 points per period/wavelength at ω_0 in fig. 12.

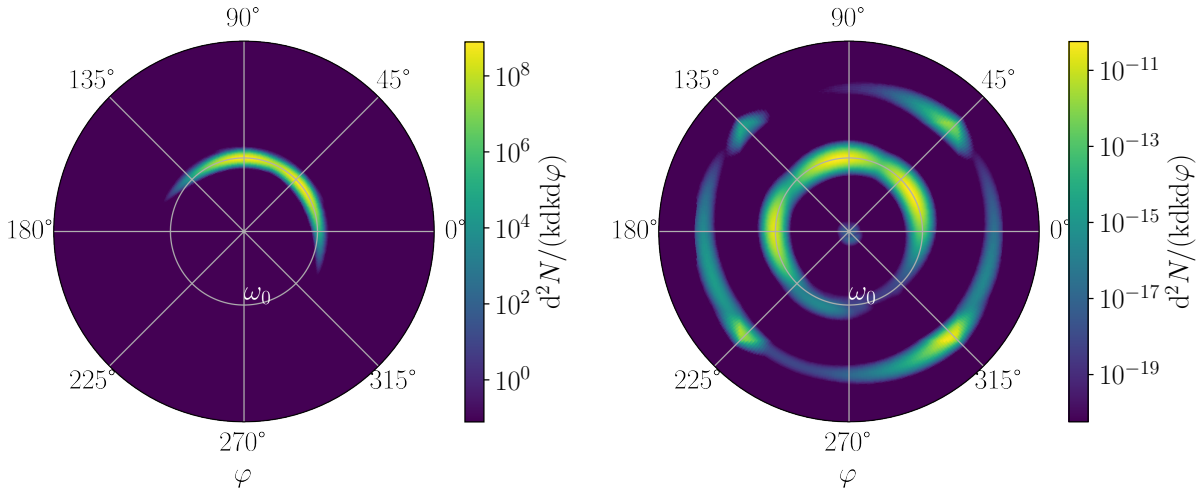

(a) Background, 3 points per period/wavelength at ω_0

(b) Signal, 3 points per period/wavelength at ω_0

Figure 12: Background and signal photon number densities for our `GaussianParaxial` example system resolving only ω_0.

We note that, as expected, $3\omega_0$ is no longer contained in the $\boldsymbol{k}$ space. The background shown in fig. 12a is sufficiently resolved, since it is only comprised of frequencies close to ω_0. It resembles fig. 7a. In contrast, the signal (fig. 12b) is dominated by numerical artifacts and completely unphysical. Neither the ω_0 signal nor higher frequency signals are correct.
In the context of resolution, the question of the convergence of the time integration also arises. The time integration is done using the simple rectangle rule; see listing 1. Nevertheless, no convergence problems have been observed, not even with the low-resolution test in fig. 12.
We recommend resolving up to $3\omega_0$ using at least 2.5 points per period/wavelength for all axes.

3.3 Improvements

In section 3.2, we have studied the only limitation of the VacEm code in solving the zero-to-one signal photon transition amplitude (2.13) - the numerical cost. This naturally defines the focus of possible improvements. The numerical cost can be split into computation time and memory usage. We managed to achieve improvements in both areas. The computation time can be drastically reduced using multi-node parallelism. The memory usage can theoretically be halved by working with single-precision floats. The latter also has the additional effect of reducing the computation time.

3.3.1 Multi-node parallelism

The VacEm code developed by Blinne makes use of parallel computation on one node. We implemented multi-node parallelism on top of the original VacEm code in order to exceed the computation power of one node and thus reduce the computation time. We identified two possibilities for multi-node parallelism in listing 1: the FFT and the time integration. The former is already parallelized on one node. It is unclear if multi-node parallelism of the FFT would improve performance. The time integration using the rectangle rule can be straightforwardly split onto multiple nodes. This is the core idea of our multi-node implementation. It is done using `MPI` [79] through `mpi4py` [80].

Let n be the number of nodes. We split the time interval into n parts of equal size. The time loop from listing 1 gets performed on each node separately for the assigned part of the time interval. After the loop we add the accumulators (`s1_n`) using a parallel scheme. The simulation is finished with lines 18 to 20 from listing 1.

The parallel scheme is a choice and not a necessity of this multi-node parallelization. The simplest alternative would be to add the results from each node to the result of the head node. This would make the data transfers a serial process. As the data size being transferred can be tens of GB for each node, this takes a significant amount of time. The parallel scheme works by transferring data from every second node to its "neighbor". This is done level by level until all data arrives at the head node. The data transfer is parallel, increasing speed and stability. The disadvantage of the parallel scheme is the restriction of the number of nodes n to a power of 2. The *Draco* cluster has a user limit of 10 nodes. This leaves us with maximum of $n = 8$ nodes. We return to the example system from fig. 11b, *i.e.* $L_t = 2 \times$ (3.30), $L_{x,y,z} =$ (3.28) and 2.5 points per period/wavelength at $3\omega_0$. The performance data of our multi-node implementation is shown in tab. 4.

Table 4: Performance of multi-node parallelism for our `GaussianParaxial` example system (section 3.2.1) using double-precision floats.

Nodes	Speedup	Effectiveness	Time in s	Memory in GB
1	1.00	100 %	5063	57
2	1.95	98 %	2590	75
4	3.17	79 %	1598	75
8	6.65	83 %	761	75

We define the speedup as $\text{speedup}_n = t_1/t_n$, where t_n is the time needed for the simulation with n nodes. The effectiveness is $\text{effectiveness}_n = \text{speedup}_n/n$. Table 4 shows that using 2 nodes leads to a speedup of 1.95, *i.e.* the simulation finished in nearly half of the original time. As mentioned earlier, halving the simulation time is theoretically the best case when using 2 nodes. The effectiveness is at 98 %. For higher node numbers, the effectiveness decreases to roughly 80 %. This decrease in effectiveness for higher node numbers is the expected behavior for any multi-node implementation. It is caused by the synchronization and data transfer between the nodes. Interestingly, the memory overhead of our multi-node implementation is independent of the number of nodes - at least for the range tested. The size of the overhead is noticeable but worth the achieved speedup. When using our multi-node implementation, we have to correct the peak memory usage (3.26) by replacing the prefactor $4/3 \approx 1.3$ with roughly 1.8. The memory in tab. 4 is allocated on each node.

Note that the performance slightly varies from run to run. This is due to nodes starting late and therefore influencing the performance statistics. Furthermore, different simulation parameters could lead to different performance results. Higher spatial grid sizes should increase the effectiveness of using more nodes, since they increase the required computation time for one time step. Table 4 shows that our multi-node implementation does work and using up to 8 nodes is useful. This may be seen as a rule of thumb. Due to the numerical cost and storage requirements, a rigorous performance study is not worthwhile.

3.3.2 Single-precision floating-point operations

After we have reduced the required simulation time in the previous section 3.3.1, we now aim to reduce the memory usage. It is the greatest bottleneck of the VacEm code. Of course, the code already provides the `low_memory_mode` option, but it does decrease the performance. According to the documentation by Blinne, it does reduce memory usage by 30 % while increasing computation time by 30 %. We do not think this is a good trade-off and use `low_memory_mode = False` throughout this work. To reduce memory usage, we opt for a very simple approach: using single-precision floats instead of `Python`'s default double-precision floats. Naturally, this means loosing precision, but this loss can be neglected as shown later in this section. A single-precision float requires 32 bit of memory, this is half of the 64 bit required by a double-precision float. Theoretically, this allows us to half the total memory usage. In addition to the reduced memory usage, we also achieve a performance increase. CPU architectures are generally optimized for single-precision float calculations.

In practice, using single-precision floats in `Python` is not always trivial. `NumPy` nicely supports different data types. The packages `NumExpr` [81] and `postpic` used by the VacEm code have proven problematic to adapt, as they default to promoting floats to double precision. Our solution is to use the single-precision float data type for all three-dimensional arrays. These arrays make up the largest part of the allocated memory. A lot of manual code changes have been required to make this possible. The results can be seen in tab. 5.

Table 5: Performance of multi-node parallelism tested for our `GaussianParaxial` example system (section 3.2.1) using single-precision floats.

Nodes	Speedup	Effectiveness	Time in s	Memory in GB
1	1.00	100 %	3631	32
2	1.96	98 %	1857	40
4	3.96	99 %	916	40
8	7.25	91 %	501	40

Similar to tab. 4, we find the same trend in the effectiveness of the results in tab. 5. The absolute values are higher than in tab. 4. This is caused by the smaller field data sizes and therefore lower overhead. We provide tab. 6 to compare the time and memory requirements using single and double-precision floats.

Table 6: Comparing single to double-precision float simulations for our `GaussianParaxial` example system (section 3.2.1)

Nodes	Time ratio	Memory ratio
1	0.72	0.56
2	0.72	0.53
4	0.57	0.53
8	0.66	0.53

Table 6 shows that for one node, we save 44 % memory and 28 % simulation time using single precision. For higher numbers of nodes these values stay roughly the same.
Comparing the one-node results for single- and double-precision floats, we find a mean relative error of 7.64×10^{-9} over the whole array `s1` that stores the signal amplitudes. This error can

be neglected compared to the analytical and artifact error. We therefore recommend using `float_precision = single` in the configuration file.

4 Flat top scattering

The `ComplexEInput` class makes the VacEm code an especially powerful tool in the study of vacuum emission amplitudes. It allows us to describe arbitrary beam profiles from experiments. The strength of numerical simulations is the ability to achieve results in regimes that are analytically inaccessible or require heavy approximations. We want to test these capabilities. After we have extensively analyzed the numerical artifacts and cost of the VacEm code in section 3, we now proceed to the scattering of flat top pulses.

By flat top pulse we refer to an EM wave with a Gaussian temporal envelope and a spatial envelope characterized by a flat top profile (Heaviside step function) in the far field. Our interest in using flat top pulses instead of pulsed Gaussian beams is motivated by experiment. The finite lenses in the optical path of experimental setups cause a flat-top-like profile of the laser pulses.

4.1 Flat tops and scattering setup

The setup of interest is inspired by Karbstein and Mosman 2020 [17]. They demonstrated how tailored laser beams achieve accessible quantum vacuum signatures. Their key idea was to circumvent the problem that the largest contribution to the signal stems from quasi-elastic scattering and is inaccessible due to the dominating background. This is done with a field-free region around the optical axis in the far field of one laser pulse. To visualize the idea, we look at the laser photon number density over the angle φ in fig. 13.

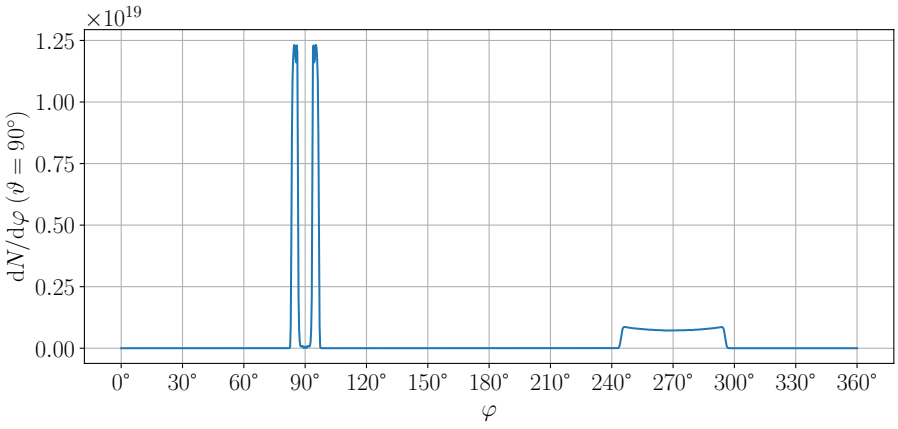

(a) Background, linear

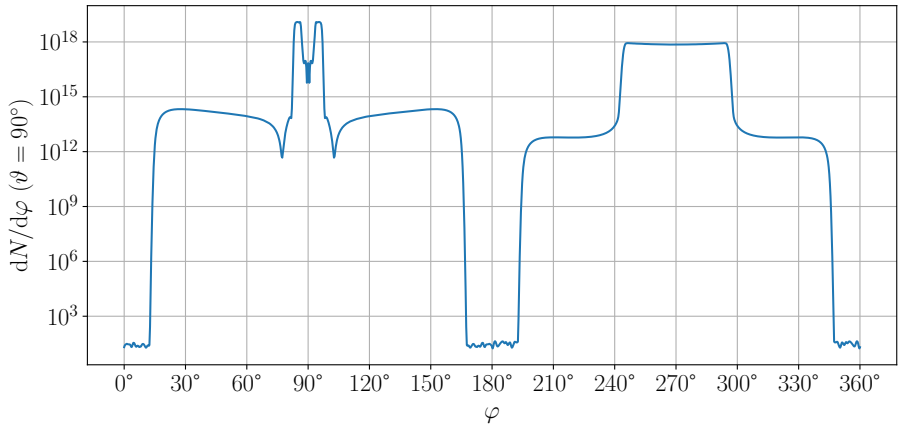

(b) Background, logarithmic

Figure 13: Background photon number density over angle φ for our flat top scattering setup with $w_{0,2} = 6 \times 10^{-7}\,\mathrm{m}$.

We see the field-free hole at $\varphi = 90°$ in fig. 13a. Furthermore, the flat-top profile of the two pulses is visible, especially for the one centered around $\varphi = 270°$. The system that fig. 13 belongs to is given by two flat top pulses, one with a hole and propagating in $+y$ direction ($\vartheta = 90°$, $\varphi = 90°$), one without a hole and propagating in $-y$ direction ($\vartheta = 90°$, $\varphi = 270°$). Both pulses have $\lambda = 800\,\mathrm{nm}$, $\tau = 34\,\mathrm{fs}$ and are polarized in z direction. They are initially constructed with a pulse energy of $W = 25\,\mathrm{J}$ each. By cutting out the hole, one beam loses a part of those 25 J. We define the hole size by $r_{\mathrm{hole}} = 70\,\mathrm{mm}$ and $r_{\mathrm{beam}} = 140\,\mathrm{mm}$, which are the respective radii at 30 cm from the focus. The flat top with hole has a beam waist of $w_{0,1} \approx 2.18 \times 10^{-6}\,\mathrm{m}$. The second pulse has $w_{0,2} = 6 \times 10^{-7}\,\mathrm{m}$ in fig. 13, but we vary this parameter throughout section 4. Similarly, we work with different simulation spacetime volumes. In the above case we used $L_t = 7\tau$, $L_{x,y,z} = 7c\tau$. Larger axis lengths would lead to an unreasonable resource demand. The grid point density stays fixed at 2.5 points per period/wavelength at $3\omega_0$, where ω_0 is now the angular frequency of the 800 nm laser pulses. The additional configuration parameters are `low_memory_mode = False`, `float_precision = 'single'` and `fieldmode = 'solver'`. The flat top pulses have been generated using code written by Fabian Schütze, PhD student of Karbstein. It was Karbstein who derived their analytical focus profile in yet unpublished work.

Figure 13b shows the major numerical challenge that we face in this section. We can not exactly resolve flat top pulses. In fact, we would need an infinitely large simulation spacetime volume and grid point density. The former is because we need infinitely many frequencies to describe a Heaviside step function and the latter because the frequencies get infinitely large. Due to the

limit in the available computational resources, we always encounter numerical artifacts when working with flat top pulses. And unlike section 3.2, the artifacts already exist in the input data. They manifest themselves most prominently in the shoulder-like structures visible in fig. 13b. They are suppressed by roughly 5 orders of magnitude. The hole depth is only 2 orders of magnitude. This gives us an indication of the error that propagates through to the signal, but keep in mind that the signal is generated from the focus region interaction and fig. 13b shows the far field. We plot the focus profiles for our flat top scattering setup with $w_{0,2} = 6 \times 10^{-7}\,\mathrm{m}$ in fig. 14.

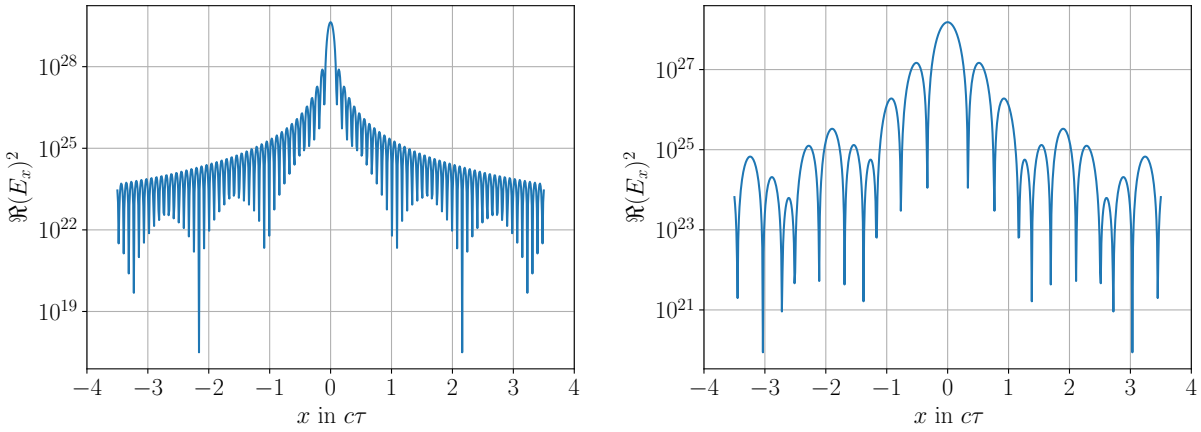

(a) Flat top without hole

(b) Flat top with hole

Figure 14: Logarithmic focus profiles for our flat top scattering setup with $w_{0,2} = 6 \times 10^{-7}\,\mathrm{m}$.

The focus profile (fig. 14) encodes the information of the flat top shape (fig. 13) in a central peak accompanied by infinitely many side peaks. Comparing fig. 14a and 14b, we see that due to the finite volume, we lose significantly more information about the flat top with hole than the one without a hole.

When scattering the flat top pulses, we are interested in the signal generated in the forward direction ($+y$ direction) of the flat top with hole (laser 1). Depending on the beam waist $w_{0,2}$ of the flat top without hole (laser 2) more or less of the side peaks of laser 1 (fig. 14b) get "illuminated", *i.e.* are a relevant part of the interaction. We mainly focus on the qualitative signal profile. The idea is that by increasing $w_{0,2}$, and thus illuminating more side peaks of the flat top with hole, the forward signal profile shape converges towards the background profile shape. It is possible to identify two limiting signal profiles and study the transition between them; see section 4.2. The signal profiles of setups similar to ours are of experimental relevance, as there is a need to optimize the signal amplitude in the background hole; *cf.* [82].

4.2 Phase transition of signal profiles

In this section, we vary the beam waist $w_{0,2}$ of the flat top without hole and study the signal of the flat top scattering in forward direction. As mentioned above, we expect two limiting cases for the signal profile shape. For $w_{0,2} \gg w_{0,1}$, we expect the signal profile shape in forward direction to resemble the background profile shape, since the side peaks of the flat top with hole are sufficiently illuminated. This is because for $w_{0,2} \to \infty$, the flat top without hole becomes fully homogeneous in the transversal directions, hence no momentum transfer can occur, and the signal therefore has the same transversal momentum and shape as the background. For $w_{0,2} \ll w_{0,1}$ only the central peak gets illuminated leading to a single-peak signal. In the picture of a scattering process: Photons change their propagation direction through scattering. We determine that the transition between these states (for the setup defined in section 4.1) occurs for $w_{0,2} \in [10^{-7}\,\mathrm{m}, 10^{-6}\,\mathrm{m}]$; *cf.* $w_{0,1} \approx 2.18 \times 10^{-6}\,\mathrm{m}$. We vary the beam waist $w_{0,2}$ in this interval with steps of $10^{-7}\,\mathrm{m}$. To visualize the transition, we show three selected signal photon number densities over φ in fig. 15.

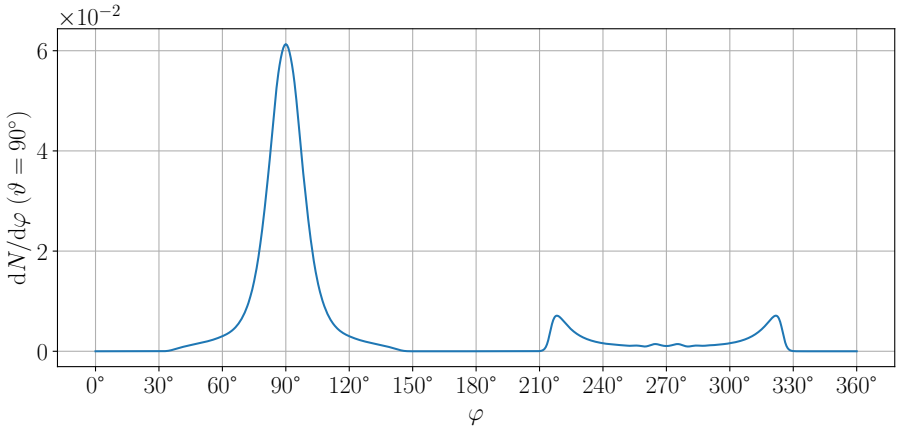

(a) Signal, $w_{0,2} = 2 \times 10^{-7}\,\mathrm{m}$

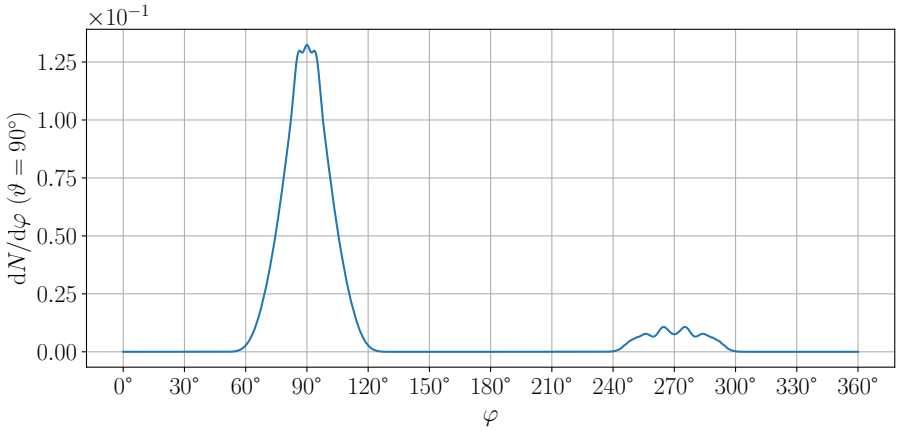

(b) Signal, $w_{0,2} = 6 \times 10^{-7}\,\mathrm{m}$

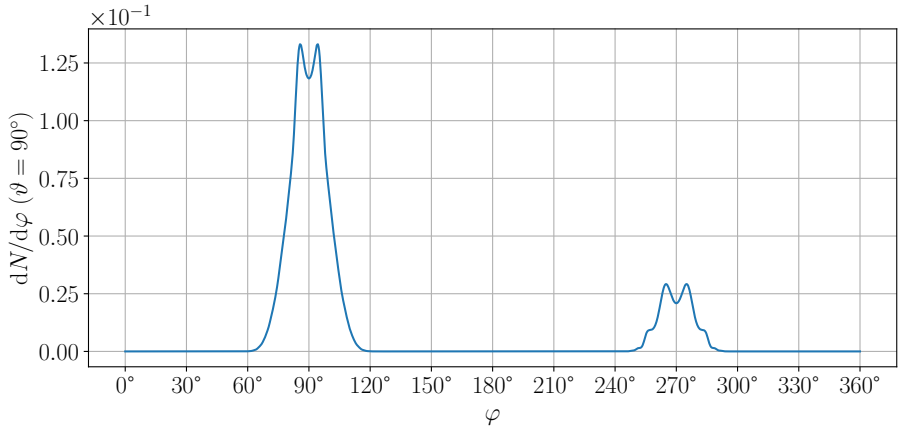

(c) Signal, $w_{0,2} = 10^{-6}\,\mathrm{m}$

Figure 15: Signal photon number densities over angle φ for our flat top scattering setup for different beam waists $w_{0,2}$.

Figure 15 shows both the forward direction signal centered around $\varphi = 90°$ and the backward direction signal centered around $\varphi = 270°$, but we are only interested in the former case. In fig. 15a, we plot the single-peak case, which qualitatively resembles the expected lower limiting case $w_{0,2} \ll w_{0,1}$. Incidentally, numerical artifacts appear for even smaller beam waists. Figure 15c features two peaks in the forward signal. Hence, we are qualitatively approaching the expected upper limiting case $w_{0,2} \gg w_{0,1}$; *cf.* fig. 13a. A transition state is shown in fig. 15b. Three peaks become visible, but the central peak still dominates.

The resulting picture is reminiscent to that of a phase transition as a function of the control parameter $w_{0,2}$ and the peak position serving as an order parameter. There is one phase where the central peak dominates and another one where the outer peaks dominate. The phase transition is shown in fig. 16.

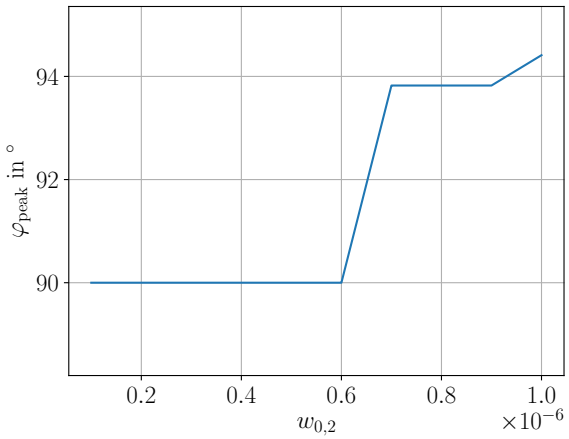

(a) Phase transition

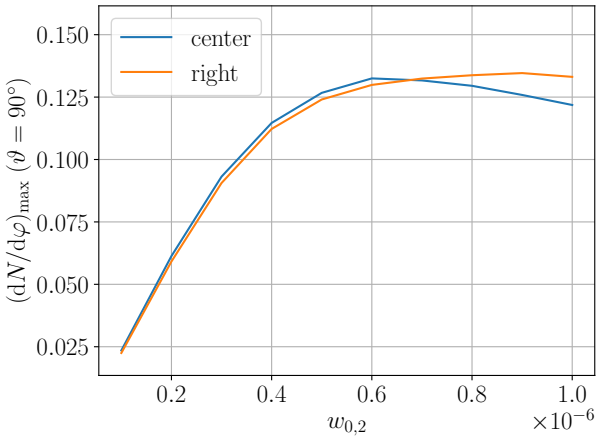

(b) Peak heights

Figure 16: Phase transition between dominating inner and outer peaks of the forward signal for our flat top scattering setup.

We observe that the phase transition is a first order phase transition. We see the discontinuous transition, characteristic for a first order phase transition, in fig. 16a. The angle φ_{peak} is the azimuthal angle at which the highest peak is centered. Therefore, $\varphi_{\text{peak}} = 90°$ characterizes the phase where the central peak dominates and $\varphi_{\text{peak}} \approx 94°$ the phase where the outer peaks dominate. There are two reasons why φ_{peak} is not constant for the latter phase. First, the central peak pulls the outer peaks inwards while growing, *i.e.* for decreasing $w_{0,2}$. Second, the flat top without hole also has side peaks in the focus region (although they are closely packed), which causes fluctuations in the interaction when varying $w_{0,2}$. Figure 16b tracks the peak heights. From the close graphs, we see that the position of the phase transition is highly susceptible to numerical artifacts. Slight changes in the graphs can significantly alter the position of the phase transition. For this reason, we settle on determining the position of the phase transition from fig. 16a. We find $w_{0,2,\text{pt},7} = (6.5 \pm 0.5) \times 10^{-7}\,\text{m}$, where "pt" stands for "phase transition" and "7" indicates $L_t = 7\tau$, $L_{x,y,z} = 7c\tau$.

Unfortunately, this result is strongly affected by numerical artifacts. Their sources are known from section 3.2 and fig. 14, and we see them manifest in fig. 13b and fig. 17.

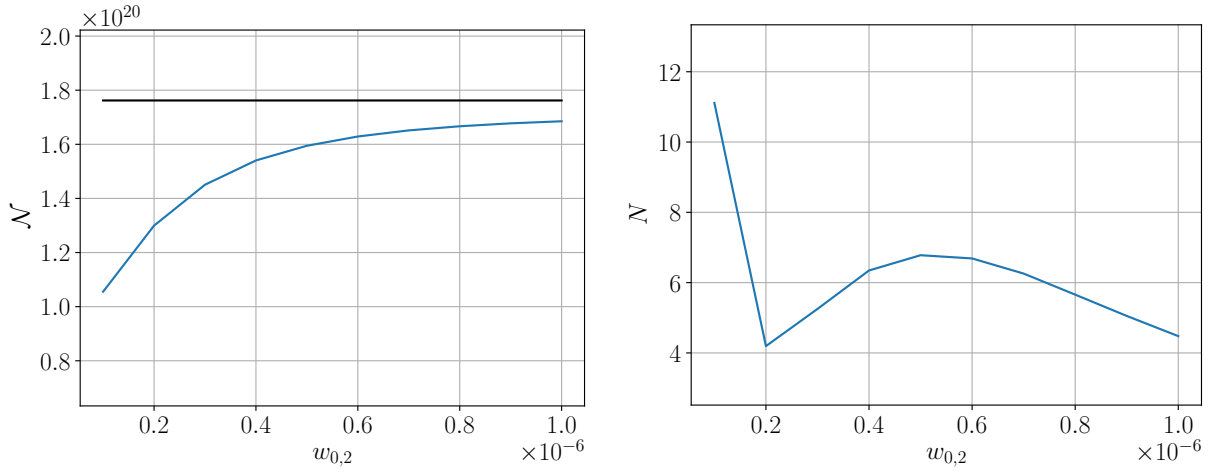

(a) Background (b) Signal

Figure 17: Background and signal total photon numbers over beam waist $w_{0,2}$ for our flat top scattering setup.

In fig. 17, we plot the total photon numbers of the background ($\mathcal{N}$) and the signal (N). For the background, we can analytically calculate the expected total photon number as

$$\tilde{\mathcal{N}} = \frac{\left[1 + \left(1 - \frac{\pi r_{\text{hole}}^2}{\pi r_{\text{beam}}^2}\right)\right] W}{\hbar\omega_0} = \frac{\left[1 + \left(1 - \left(\frac{140\times10^{-3}\,\text{m}}{70\times10^{-3}\,\text{m}}\right)^2\right)\right] \times 25\,\text{J}}{\frac{hc}{8\times10^{-7}\,\text{m}}} = 1.762 \times 10^{20}\,. \tag{4.1}$$

We see that $\tilde{\mathcal{N}}$ is independent of $w_{0,2}$ as it should be, and we mark the constant value with black in fig. 17a. The simulation results (blue) deviate for small beam waist up to 35 % from the expected constant. It is caused by the fixed grid point density, which is unable to resolve the increasing frequencies that emerge when decreasing $w_{0,2}$. This could also explain the unexpectedly high number of signal photons for $w_{0,2} = 10^{-7}\,\text{m}$ in fig. 17b. Fortunately, these artifacts are just a rescaling of the energy and should not have a qualitative impact on the phase transition. We see the finite volume as the main problem when studying the phase transition. The position of the phase transition is highly susceptible to small variations in the signal, and we also desire to achieve quantitatively accurate results for future studies. Section 4.3 therefore deals with extrapolating towards infinite simulation spacetime volume.

Concerning fig. 17b, note that the maximum signal is not achieved at $w_{0,2} = 5 \times 10^{-7}\,\text{m}$ (this is just a local maximum) but lies at higher beam waist.

4.3 Extrapolation towards infinite simulation spacetime volume

Since numerical discretization artifacts can currently not be fully suppressed by pure computational power, let us study the approach to the continuum in order to estimate the errors and to extrapolate to the continuum. We focus on extrapolating the results of our flat top scattering setup towards infinite simulation spacetime volume. This means infinite $\boldsymbol{k}$ space resolution; *i.e.* a continuous $\boldsymbol{k}$ space. To acquire the data for the extrapolation, we repeat the simulation from section 4.2 for different spacetime volumes $L_t = \zeta \times \tau$, $L_{x,y,z} = \zeta \times c\tau$, where $\zeta \in \{1, 1.5, 2, 3, 4, 5, 6, 7\}$. We keep the grid point density fixed at 2.5 points per wavelength at $3\omega_0$; *i.e.* no continuous position space. We plot the results over ζ^{-1}; *e.g.* fig. 18 for $w_{0,2} = 6 \times 10^{-7}\,\mathrm{m}$.

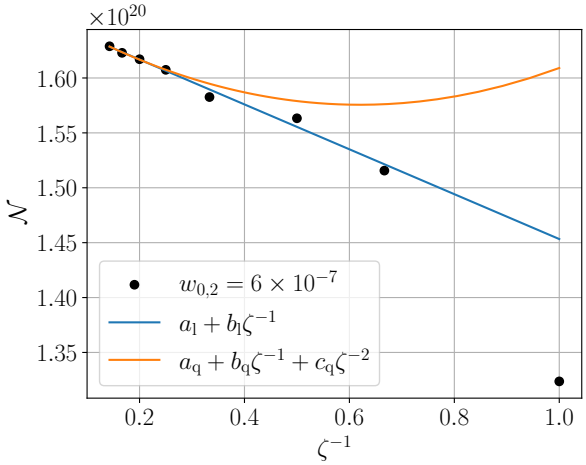

(a) Background

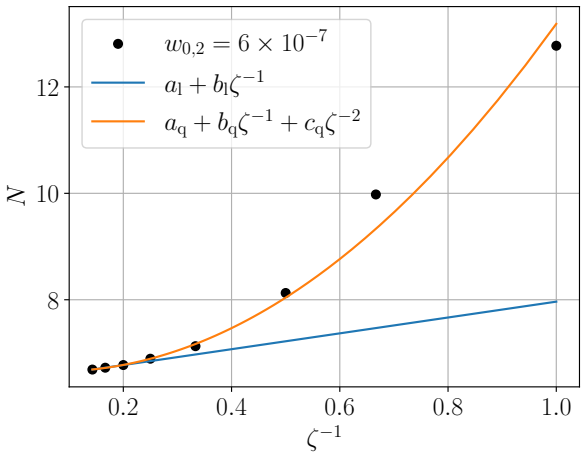

(b) Signal

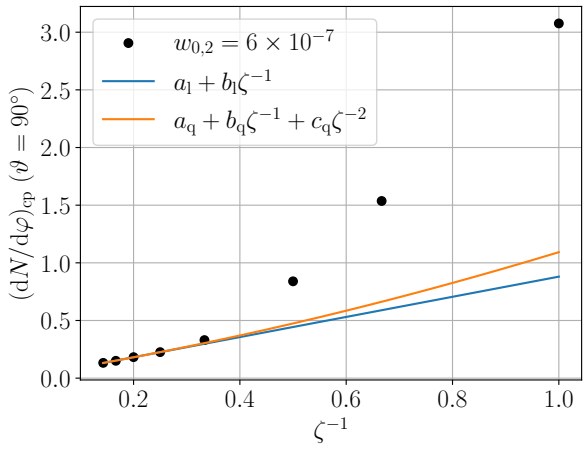

(c) Central peak

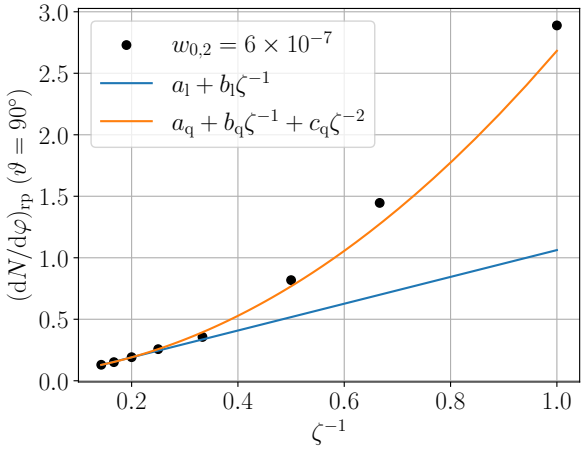

(d) Right peak

Figure 18: Variation of the simulation spacetime volume for our flat top scattering setup with $w_{0,2} = 6 \times 10^{-7}\,\mathrm{m}$.

We have chosen to plot over the inverse of the volume parameter ζ, because it simplifies the asymptotic behavior of the results. When fitting the results, the assumption is that the finite volume numerical artifacts can be expanded like $a + b\zeta^{-1} + c\zeta^{-2} + \mathcal{O}\left(\zeta^{-3}\right)$. We fit linear through the first three data points and quadratic through the first four data points (linear or quadratic with respect to ζ^{-1}). This is the smallest number of data points that gives us an error for the fitting parameters. *A priori*, it is unclear if the first three data points have a large enough ζ to justify the linear fit or if the results are still in a regime that would require a higher order polynomial (analogously for the quadratic fit). For the fits to reasonably describe the asymptotic behavior ($\zeta \to \infty$), we require that a_7, a_l, a_q are all sufficiently close. a_7 is the result at $\zeta = 7$, a_l is the result for linear extrapolation, and a_q is the result for quadratic extrapolation. Table 7 shows the comparison of the parameter a for the example beam waist in fig. 18.

Table 7: Comparison of parameter a for an assessment of fit suitability for extrapolation.

	$\mathcal{N}$	N	$\left(\frac{\mathrm{d}N}{\mathrm{d}\varphi}\right)_\mathrm{cp}(\vartheta = 90°)$	$\left(\frac{\mathrm{d}N}{\mathrm{d}\varphi}\right)_\mathrm{rp}(\vartheta = 90°)$
a_7	1.6289×10^{20}	6.6880	0.132	0.130
a_l	$(1.6577 \pm 0.0072) \times 10^{20}$	6.4750 ± 0.0043	0.007 ± 0.018	-0.027 ± 0.029
a_q	$(1.6651 \pm 0.0222) \times 10^{20}$	6.6919 ± 0.1385	0.018 ± 0.062	0.044 ± 0.061

The error values belong to a 95 % confidence interval ($\pm 2\sigma$). We see in tab. 7 that for the total photon numbers $\mathcal{N}$, N our loosely defined closeness requirement is satisfactorily fulfilled. For the peak heights, the requirement is clearly violated. We even encounter a negative density, which, of course, is a numerical artifact of the extrapolation. This indicates that the finite volume artifacts have a significantly smaller impact on the total photon numbers than on the peak heights.

To get the full picture, we show the extrapolated versions of fig. 16 and 17 in fig. 19.

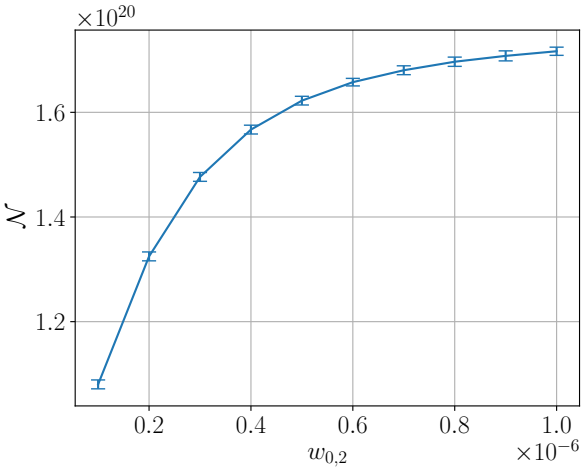

(a) Background, linear

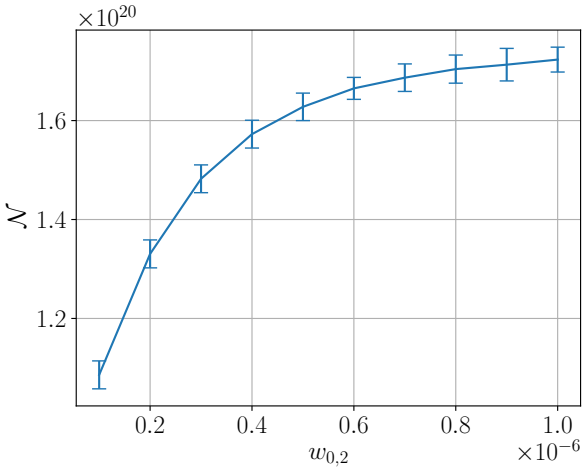

(b) Background, quadratic

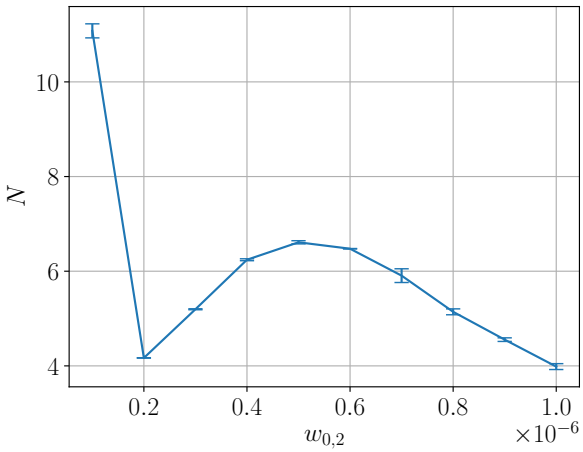

(c) Signal, linear

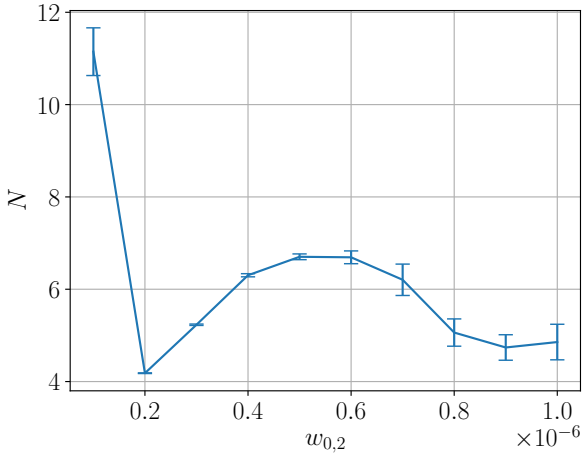

(d) Signal, quadratic

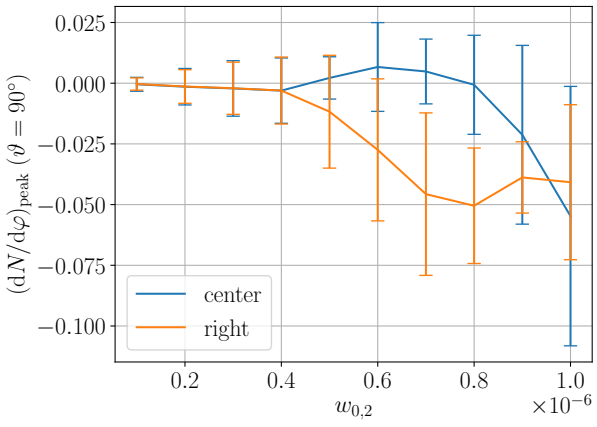

(e) Peak heights, linear

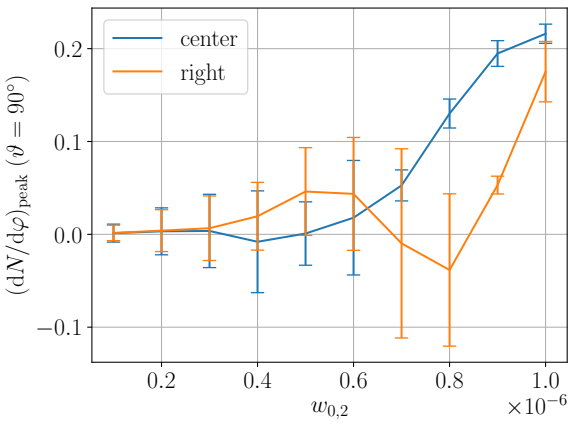

(f) Peak heights, quadratic

Figure 19: Linear and quadratic extrapolation towards infinite simulation spacetime volume for our flat top scattering setup.

The extrapolated plots for the background and signal total photon numbers (fig. 19a to 19d) look similar to fig. 17. This again supports our claim that the remaining artifacts at $\zeta = 7$ in the total photon numbers are mainly caused by the finite grid point density and not the finite volume. We also see that the linear fit performs more precise than the quadratic fit. Hence, we conclude that the data points are in fact in the linear regime. The impact of finite volume artifacts is sufficiently small, such that we can successfully extrapolate them away.
In fig. 19e and 19f this extrapolation fails. We have large error bars, negative densities and nonsensical graphs in contradiction to the expected qualitative behavior from fig. 16b. Apparently, the data points are neither in the linear nor in the quadratic regime. The finite volume numerical artifacts are not sufficiently suppressed for the used data points. Multiple data points for $\zeta > 7$ would be required for the above method to work. The extrapolated peak heights do not provide insight into the phase transition. Still there is an alternative to determine the position of the phase transition at infinite simulation spacetime volume. We can determine the position for different ζ from plots like fig. 16a. From such a procedure, we obtain fig. 20.

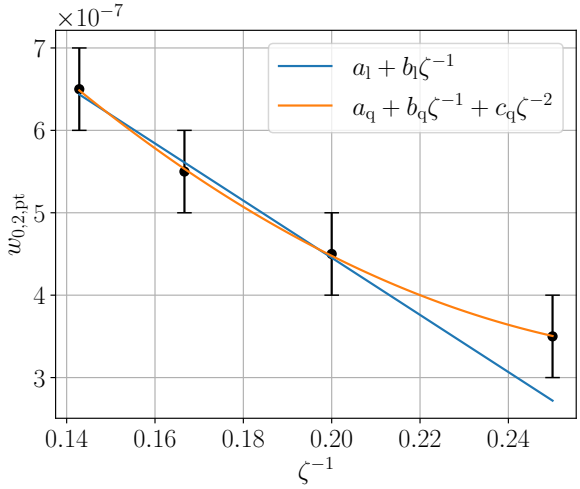

Figure 20: Position of the phase transition over the inverse simulation spacetime volume parameter ζ^{-1} for our flat top scattering setup.

Table 8: Extrapolation results of the phase transition position.

	$w_{0,2,\mathrm{pt}}$
a_7	$(0.65 \pm 0.05) \times 10^{-6}\,\mathrm{m}$
a_l	$(1.14 \pm 0.11) \times 10^{-6}\,\mathrm{m}$
a_q	$(1.57 \pm 0.13) \times 10^{-6}\,\mathrm{m}$

Fitting the data analogous to fig. 18, we find the linear (a_l) and quadratic (a_q) extrapolation results in tab. 8. Again, the values for a_7, a_l, a_q are not as close as desired, but close enough to give a reasonable estimate of the phase transition position $w_{0,2,\mathrm{pt}}$. Judging from fig. 20, the data points are assumed to be in the quadratic regime. Therefore, we expect the phase transition

for infinite simulation spacetime volume to happen at $w_{0,2,\mathrm{pt}} \approx a_\mathrm{q} = (1.57 \pm 0.13) \times 10^{-6}\,\mathrm{m}$. Remember that this result is still affected by finite grid point density numerical artifacts.

Section 4.3 has shown that we are working at the frontier of the current computational resources and algorithms. Eliminating numerical artifacts through extrapolation does work but only when they are already sufficiently small. Due to the computational limitations, it has to be seen on a case to case basis if this regime can be entered.

We have successfully explored the frontier of numerical simulations of the vacuum emission process. The VacEm code plus the improvements made in section 3.3 enable the study of previously inaccessible regimes; *e.g.* scattering of flat top pulses beyond typical approximations used in analytical estimates.

5 Conclusion

In this work, we studied the VacEm code by Blinne, showed its capabilities and limitations, made improvements, and employed it to simulate previously unexplored regimes of the vacuum emission process. The core of this process (2.14) is the signal amplitude (2.13). Solving it poses a challenge whose difficulty depends on the EM background fields (lasers). With the goal of calculating the signal amplitude for realistic experimental setups, the need for numerical simulations arises.

After introducing the necessary theoretical background in section 2, we studied the inner workings of the VacEm code in detail; see section 3. This includes the reformulation of the signal amplitude for efficient computation in section 3.1.1, the simulation algorithm and its memory usage in section 3.1.2, and the class structure and workflow in section 3.1.3. These sections may be seen as a technical handbook to using the VacEm code. Analyzing the memory usage showed that extensive memory requirements are the main limitation of the VacEm code (tab. 1). Therefore, it is of great importance to choose simulation parameters that achieve accurate results while minimizing memory usage. This was the topic of section 3.2. We showed finite volume and finite grid point density numerical artifacts. For pulsed Gaussian beams we derived an optimal parameter set. Unfortunately, the simulation spacetime volume (3.28) to (3.30) is inversely proportional to the wavelength. The simulations in this work for 800 nm lasers are already close to the resource limit. Code improvements are desired, especially with regard to X-ray free electron lasers (XFEL) that show great promise [25, 27, 83, 84]. We implemented two improvements to the VacEm code in section 3.3. They tackle both memory usage and computation time. First, multi-node parallelism was implemented through MPI and allows to divide the computation time by the number of nodes; see section 3.3.1. Second, we added the option of single-precision float computations, which saves roughly half the memory and a quarter of the computation time. The loss in precision is negligible compared to the analytical and artifact error. The performance of our improvements can be seen in tab. 4 and 5.

Thanks to the improvements, we were able to leave behind the regime of Gaussian beams and show a proof of concept for numerical simulations of flat top scattering in section 4. Flat tops pose a great challenge due to the infinite frequencies involved. Nevertheless, we were able to find a phase transition between two distinct signal profiles (fig. 16a). This feature was assumed to be there but not yet analyzed in detail when scattering a flat top with hole and one without hole. To manage the inevitably strong artifacts when simulating flat top pulses, we used ex-

trapolation towards infinite simulation spacetime volume (infinite $\boldsymbol{k}$ space resolution). This was only partly successful (fig. 19e and 19f), since we are working at the frontier of computational capabilities. Also, we did only resolve the finite volume artifacts. The finite grid point density artifacts remain. It should be possible to deal with those in a similar fashion.

We recommend an extrapolation towards infinite grid point density for a future study. There is great potential in the VacEm code for guiding experiments in the search of non-linear signatures of the QED quantum vacuum. Our code improvements are only a small step in optimizing the simulation. The understanding gained in this work provides a strong foundation for further performance enhancements. We see possibilities to streamline the algorithm to require less memory and operations. As the VacEm code is only limited by computational cost, this would broaden the set of systems to simulate and insight to gain. Furthermore, it would allow for more quantitatively accurate result, a quality strongly desired when comparing theory and experiment.

Already in its current state, the VacEm code can be deployed to countless systems elusive to analytical study. With the growing accessibility of the QED vacuum in experiment, the VacEm code could proof to be a valuable tool for signal predictions.

6 Appendix

A Abbreviations

QFT	quantum field theory
QED	quantum electrodynamics
VEP	vacuum emission picture
ED	electrodynamics
HPC	high-performance computing
EOM	equations of motion
LCFA	locally constant field approximation
DOF	degree(s) of freedom
FFT	fast Fourier transform
iFFT	inverse fast Fourier transform
XFEL	X-ray free electron lasers

B List of figures

C List of tables

D List of listings

E References

[1] J. C. Maxwell, *A Treatise on Electricity and Magnetism*, Vol. 1, 2 vols. (Clarendon Press, 1873).

[2] R. P. Feynman, M. Sands, and R. B. Leighton, *The Feynman Lectures on Physics*, Vol. 2 (Basic Books, New York, 2013).

[3] R. P. Feynman, *QED: The Strange Theory of Light and Matter* (Princeton University Press, 1985).

[4] M. Inman, "In search of alpha", New Scientist **191**, 40 (2006).

[5] W. Dittrich and H. Gies, *Probing the quantum vacuum: pertubative effective action aproach in quantum electrodynamics and its application*, Vol. 166, Springer Tracts in Modern Physics (Springer, Berlin, 2000).

[6] D. Strickland and G. Mourou, "Compression of amplified chirped optical pulses", Optics Communications **55**, 447 (1985).

[7] D. Strickland, P. Maine, M. Bouvier, S. Williamson, and G. Mourou, "Picosecond Pulse Amplification Using Pulse Compression Techniques", in Topical Meeting on Ultrafast Phenomena (June 16, 1986).

[8] M. Pessot, P. Maine, and G. Mourou, "1000 times expansion/compression of optical pulses for chirped pulse amplification", Optics Communications **62**, 419 (1987).

[9] P. Maine, D. Strickland, P. Bado, M. Pessot, and G. Mourou, "En route vers le Petawatt", Rev. Phys. Appl. (Paris) **22**, 1657 (1987).

[10] P. Maine, D. Strickland, P. Bado, M. Pessot, and G. Mourou, "Generation of ultrahigh peak power pulses by chirped pulse amplification", IEEE Journal of Quantum Electronics **24**, 398 (1988).

[11] H. Euler and B. Kockel, "Über die Streuung von Licht an Licht nach der Diracschen Theorie", Naturwissenschaften **23**, 246 (1935).

[12] W. Heisenberg and H. Euler, "Folgerungen aus der Diracschen Theorie des Positrons", Z. Physik **98**, 714 (1936).

[13] G. V. Dunne, "The Heisenberg-Euler Effective Action: 75 years on", Int. J. Mod. Phys. A **27**, 1260004 (2012).

[14] F. Karbstein, "The quantum vacuum in electromagnetic fields: From the Heisenberg-Euler effective action to vacuum birefringence", Helmholtz International Summer School 2016, 10.3204/DESY-PROC-2016-04 (2017).

[15] F. Karbstein, "Probing vacuum polarization effects with high-intensity lasers", Particles **3**, 39 (2020).

[16] A. Fedotov, A. Ilderton, F. Karbstein, B. King, D. Seipt, H. Taya, and G. Torgrimsson, "Advances in QED with intense background fields", Physics Reports, Advances in QED with Intense Background Fields **1010**, 1 (2023).

[17] F. Karbstein and E. A. Mosman, "Enhancing quantum vacuum signatures with tailored laser beams", Phys. Rev. D **101**, 113002 (2020).

[18] Z. Bialynicka-Birula and I. Bialynicki-Birula, "Nonlinear Effects in Quantum Electrodynamics. Photon Propagation and Photon Splitting in an External Field", Phys. Rev. D **2**, 2341 (1970).

[19] S. L. Adler, "Photon splitting and photon dispersion in a strong magnetic field", Annals of Physics **67**, 599 (1971).

[20] E. B. Aleksandrov, A. A. Ansel'm, and A. N. Moskalev, "Vacuum birefringence in an intense laser radiation field", Sov. Phys. JETP **62** (1985).

[21] G. L. Kotkin and V. G. Serbo, "Polarization of high-energy -quanta traversing a bunch of polarized laser photons", Physics Letters B **413**, 122 (1997).

[22] T. Heinzl, B. Liesfeld, K.-U. Amthor, H. Schwoerer, R. Sauerbrey, and A. Wipf, "On the observation of vacuum birefringence", Optics Communications **267**, 318 (2006).

[23] V. Dinu, T. Heinzl, A. Ilderton, M. Marklund, and G. Torgrimsson, "Vacuum refractive indices and helicity flip in strong-field QED", Phys. Rev. D **89**, 125003 (2014).

[24] F. Karbstein, H. Gies, M. Reuter, and M. Zepf, "Vacuum birefringence in strong inhomogeneous electromagnetic fields", Phys. Rev. D **92**, 071301 (2015).

[25] H.-P. Schlenvoigt, T. Heinzl, U. Schramm, T. E. Cowan, and R. Sauerbrey, "Detecting vacuum birefringence with x-ray free electron lasers and high-power optical lasers: a feasibility study", Phys. Scr. **91**, 023010 (2016).

[26] A. Ilderton and M. Marklund, "Prospects for studying vacuum polarisation using dipole and synchrotron radiation", Journal of Plasma Physics **82**, 655820201 (2016).

[27] F. Karbstein and C. Sundqvist, "Probing vacuum birefringence using x-ray free electron and optical high-intensity lasers", Phys. Rev. D **94**, 013004 (2016).

[28] B. King and N. Elkina, "Vacuum birefringence in high-energy laser-electron collisions", Phys. Rev. A **94**, 062102 (2016).

[29] Y. Nakamiya and K. Homma, "Probing vacuum birefringence under a high-intensity laser field with gamma-ray polarimetry at the GeV scale", Phys. Rev. D **96**, 053002 (2017).

[30] S. Bragin, S. Meuren, C. H. Keitel, and A. Di Piazza, "High-Energy Vacuum Birefringence and Dichroism in an Ultrastrong Laser Field", Phys. Rev. Lett. **119**, 250403 (2017).

[31] R. Karplus and M. Neuman, "The Scattering of Light by Light", Phys. Rev. **83**, 776 (1951).

[32] J. Mckenna and P. M. Platzman, "Nonlinear Interaction of Light in a Vacuum", Phys. Rev. **129**, 2354 (1963).

[33] A. A. Varfolomeev, "Induced scattering of light by light", Sov. Phys. JETP **23** (1966).

[34] N. N. Rozanov, "Four-wave interactions of intense radiation in vacuum", Sov. Phys. JETP **76** (1993).

[35] F. Moulin and D. Bernard, "Four-wave interaction in gas and vacuum: definition of a third-order nonlinear effective susceptibility in vacuum: vacuum(3)", Optics Communications **164**, 137 (1999).

[36] E. Lundström, G. Brodin, J. Lundin, M. Marklund, R. Bingham, J. Collier, J. T. Mendonça, and P. Norreys, "Using High-Power Lasers for Detection of Elastic Photon-Photon Scattering", Phys. Rev. Lett. **96**, 083602 (2006).

[37] D. Tommasini and H. Michinel, "Light by light diffraction in vacuum", Phys. Rev. A **82**, 011803 (2010).

[38] B. King, A. Di Piazza, and C. H. Keitel, "A matterless double slit", Nature Photon **4**, 92 (2010).

[39] B. King and C. H. Keitel, "Photon–photon scattering in collisions of intense laser pulses", New J. Phys. **14**, 103002 (2012).

[40] H. Gies, F. Karbstein, and C. Kohlfürst, "All-optical signatures of strong-field QED in the vacuum emission picture", Phys. Rev. D **97**, 036022 (2018).

[41] H. Gies, F. Karbstein, C. Kohlfürst, and N. Seegert, "Photon-photon scattering at the high-intensity frontier", Phys. Rev. D **97**, 076002 (2018).

[42] B. King, H. Hu, and B. Shen, "Three-pulse photon-photon scattering", Phys. Rev. A **98**, 023817 (2018).

[43] F. Karbstein, A. Blinne, H. Gies, and M. Zepf, "Boosting Quantum Vacuum Signatures by Coherent Harmonic Focusing", Phys. Rev. Lett. **123**, 091802 (2019).

[44] V. P. Yakovlev, "Incoherent electromagnetic wave scattering in a Coulomb field", Sov. Phys. JETP **24** (1967).

[45] H. Gies, F. Karbstein, and R. Shaisultanov, "Laser photon merging in an electromagnetic field inhomogeneity", Phys. Rev. D **90**, 033007 (2014).

[46] H. Gies, F. Karbstein, and N. Seegert, "Photon merging and splitting in electromagnetic field inhomogeneities", Phys. Rev. D **93**, 085034 (2016).

[47] S. L. Adler, J. N. Bahcall, C. G. Callan, and M. N. Rosenbluth, "Photon Splitting in a Strong Magnetic Field", Phys. Rev. Lett. **25**, 1061 (1970).

[48] R. J. Stoneham, "Phonon splitting in the magnetised vacuum", J. Phys. A: Math. Gen. **12**, 2187 (1979).

[49] V. N. Baier, A. I. Milshtein, and R. Zh. Shaisultanov, "Photon splitting in a strong electromagnetic field", Zhurnal Eksperimentalnoi i Teoreticheskoi Fiziki **90**, 1141 (1986).

[50] S. L. Adler and C. Schubert, "Photon Splitting in a Strong Magnetic Field: Recalculation and Comparison with Previous Calculations", Phys. Rev. Lett. **77**, 1695 (1996).

[51] R. N. Lee, A. I. Milstein, and V. M. Strakhovenko, "High-energy photon splitting on heavy atoms", Phys. Rev. A **57**, 2325 (1998).

[52] A. Di Piazza, A. I. Milstein, and C. H. Keitel, "Photon splitting in a laser field", Phys. Rev. A **76**, 032103 (2007).

[53] Z. Bialynicka-Birula, "Nonlinear phenomena in the propagation of electromagnetic waves in the magnetzed vacuum", Physica D: Nonlinear Phenomena **2**, 513 (1981).

[54] A. Di Piazza, K. Z. Hatsagortsyan, and C. H. Keitel, "Harmonic generation from laser-driven vacuum", Phys. Rev. D **72**, 085005 (2005).

[55] A. M. Fedotov and N. B. Narozhny, “Generation of harmonics by a focused laser beam in the vacuum”, Physics Letters A **362**, 1 (2007).

[56] P. Böhl, B. King, and H. Ruhl, “Vacuum high-harmonic generation in the shock regime”, Phys. Rev. A **92**, 032115 (2015).

[57] H. Kadlecová, G. Korn, and S. V. Bulanov, “Electromagnetic shocks in the quantum vacuum”, Phys. Rev. D **99**, 036002 (2019).

[58] F. Karbstein and R. Shaisultanov, “Stimulated photon emission from the vacuum”, Phys. Rev. D **91**, 113002 (2015).

[59] H. Gies, F. Karbstein, and L. Klar, “All-optical Quantum Vacuum Signals in Two-Beam Collision”, Phys. Rev. D **106**, 116005 (2022).

[60] C. Sundqvist and F. Karbstein, *Two-beam laser photon merging*, (Mar. 21, 2023) https://arxiv.org/abs/2303.11904 (visited on 07/17/2023), preprint.

[61] A. Blinne, H. Gies, F. Karbstein, C. Kohlfürst, and M. Zepf, “All-optical signatures of quantum vacuum nonlinearities in generic laser fields”, Phys. Rev. D **99**, 016006 (2019).

[62] *HPC-Cluster Draco*, https://wiki.uni-jena.de/pages/viewpage.action?pageId=22453002 (visited on 07/18/2023).

[63] H. Gies and F. Karbstein, “An addendum to the Heisenberg-Euler effective action beyond one loop”, J. High Energ. Phys. **2017**, 108 (2017).

[64] W. H. Furry, “A Symmetry Theorem in the Positron Theory”, Phys. Rev. **51**, 125 (1937).

[65] M. Buchanan, “Past the Schwinger limit”, Nature Phys **2**, 721 (2006).

[66] J. Schwinger, “On Gauge Invariance and Vacuum Polarization”, Phys. Rev. **82**, 664 (1951).

[67] L. Klar, “Quantum Vacuum Nonlinearities in the All-Optical Regime” (Friedrich-Schiller-Universität Jena, Jena, 2022).

[68] A. Blinne, S. Kuschel, S. Tietze, and M. Zepf, “Efficient retrieval of phase information from real-valued electromagnetic field data”, Journal of Computational Physics: X **1**, 100019 (2019).

[69] *Postpic*, https://github.com/skuschel/postpic (visited on 07/18/2023).

[70] *Mammoth | HPC @ LLNL*, https://hpc.llnl.gov/hardware/compute-platforms/mammoth (visited on 09/06/2023).

[71] A. Blinne, H. Gies, F. Karbstein, C. Kohlfürst, and M. Zepf, "The Vacuum Emission Picture Beyond Paraxial Approximation", J. Phys.: Conf. Ser. **1206**, 012017 (2019).

[72] *Pylint*, https://pylint.org/ (visited on 09/07/2023).

[73] *Graphviz*, https://graphviz.org/ (visited on 09/07/2023).

[74] Y. Salamin, "Fields of a Gaussian beam beyond the paraxial approximation", Appl. Phys. B **86**, 319 (2007).

[75] W. J. Waters and B. King, "On beam models and their paraxial approximation", Laser Phys. **28**, 015003 (2017).

[76] S. Gales, K. A. Tanaka, D. L. Balabanski, F. Negoita, D. Stutman, O. Tesileanu, C. A. Ur, D. Ursescu, I. Andrei, S. Ataman, M. O. Cernaianu, L. D'Alessi, I. Dancus, B. Diaconescu, N. Djourelov, D. Filipescu, P. Ghenuche, D. G. Ghita, C. Matei, K. Seto, M. Zeng, and N. V. Zamfir, "The extreme light infrastructure - nuclear physics (ELI-NP) facility: new horizons in physics with 10 PW ultra-intense lasers and 20 MeV brilliant gamma beams", Rep. Prog. Phys. **81**, 094301 (2018).

[77] *ELI-NP*, https://www.eli-np.ro/ro/user_facilities.php (visited on 07/18/2023).

[78] C. Shannon, "Communication in the Presence of Noise", Proceedings of the IRE **37**, 10 (1949).

[79] *Open MPI*, https://www.open-mpi.org/ (visited on 07/25/2023).

[80] *Mpi4py*, https://github.com/mpi4py/mpi4py (visited on 07/25/2023).

[81] *NumExpr*, https://github.com/pydata/numexpr (visited on 07/26/2023).

[82] F. Karbstein, D. Ullmann, E. A. Mosman, and M. Zepf, "Direct accessibility of the fundamental constants governing light-by-light scattering", Phys. Rev. Lett. **129**, 061802 (2022).

[83] F. Karbstein, "Vacuum birefringence in the head-on collision of x-ray free-electron laser and optical high-intensity laser pulses", Phys. Rev. D **98**, 056010 (2018).

[84] F. Karbstein and E. A. Mosman, "X-ray photon scattering at a focused high-intensity laser pulse", Phys. Rev. D **100**, 033002 (2019).

F Danksagung

Mein großer Dank gilt Professor Holger Gies. Ich danke Ihnen für die Möglichkeit dieser Masterarbeit zwischen Theorie, Informatik und Experiment. Sie haben sich Zeit genommen für meine unzähligen Fragen und Probleme. Ich bin sehr dankbar für Ihre ruhige und vorausschauende Betreuung.
Ich danke auch Dr. Felix Karbstein, dem Zweitkorrektor dieser Arbeit. Auf Ihrem theoretischen Fundament steht meine Arbeit und ich danke Ihnen für Gespräche und Unterstützung.
Fabian Schütze hat mir im regen Austausch vielerlei Wissen vermittelt und zum Gelingen dieser Arbeit beigetragen. Ebenfalls unterstützte mich Chantal Sundqvist. Vielen Dank euch beiden.
Ein besonderer Dank gebührt meiner Familie und meiner Freundin für ihre bedingungslose Unterstützung.

G Eigenständigkeitserklärung

Ich erkläre, dass ich die vorliegende Arbeit selbständig und nur unter Verwendung der angegebenen Hilfsmittel und Quellen angefertigt habe. Die eingereichte Arbeit ist nicht anderweitig als Prüfungsleistung verwendet worden oder in englischer oder einer anderen Sprache als Veröffentlichung erschienen.

Seitens des Verfassers bestehen keine Einwände, die vorliegende Masterarbeit für die öffentliche Benutzung zur Verfügung zu stellen.

Jena, den 12.09.2023

Lars Maiwald